Theoretical Notes

Note 352

July 1984

Air Chemistry Measurements II

D.K. Davies and P.J. Chantry
Westinghouse Electric Corporation

Abstract

    This report describes a comprehensive set of measurements of electron, negative-ion, and positive-ion mobilities together with attachment and ionization rate coefficients for dry air and mixtures of dry air with water vapor. These measurements were made for values of E/N (the ratio of electric field to gas density) ranging from $\sim 10^{-22}$ Vm^2 to $\sim 3 \times 10^{-19}$ Vm^2. This range of E/N corresponds to values of electric field at atmospheric pressure from $\sim 10^4$ to $\sim 10^7$ V/m and covers values of electron mean energy from near thermal to values well above the onset of impact ionization.

PREFACE

This final report was prepared by the Westinghouse R&D Center, 1310 Beulah Road, Pittsburgh, PA 15235, under Subcontract No. DC-SC-2030-1 from Dikewood, Division of Kaman Sciences Corporation, Albuquerque, NM 87102, with C. W. Jones as Project Monitor. The technical effort described in this report was conducted by D. K. Davies and P. J. Chantry and accomplished during the period 11 January 1983 through 30 April 1984. Thanks are due to W. M. Uhlig and L. D. Kurtz for their fine technical support.

CONTENTS

I. INTRODUCTION

The objective of this program is to provide a comprehensive set of measurements of electron, negative-ion, and positive-ion mobilities together with attachment and ionization rate coefficients for dry air and mixtures of dry air with water vapor. To cover the range of electric fields encountered during the period of air conductivity following an electromagnetic pulse event, these measurements are made for values of E/N (the ratio of electric field to gas density) ranging from $\sim 10^{-22}$ Vm^2 to $\sim 3 \times 10^{-19}$ Vm^2. This range of E/N corresponds to values of electric field at atmospheric pressure from $\sim 10^4$ to $\sim 10^7$ V/m and covers values of electron mean energy from near thermal to values well above the onset of impact ionization.

The specific tasks addressed in the present phase of the program include completion of measurements in dry air and documentation of all the data determined for dry air.[*] In this present report we describe work carried out on the remaining tasks in this phase, the alignment and calibration of the optical absorption cell for monitoring water vapor concentrations in the drift tube, and the measurement of swarm parameters in a mixture of 2% H_2O in dry air. For the latter task, measurements have been carried out over the same range, $6 \times 10^{-22} < E/N < 3 \times 10^{-19}$ Vm^2, as that covered for the measurements in dry air.

---

[*]The results of this work have been issued in Theoretical Note 346, May 1983.

II. EXPERIMENTAL APPROACH

1. GENERAL METHODOLOGY

The method adopted for determining the electron and ion swarm
parameters in humid air is the time-resolved measurement of electron and
ion waveforms using a pulsed drift tube. In this method, a pulse of
electrons is injected from the cathode into a region of uniform electric
field E containing a gas of known density N. In general, a distribution
of electrons, negative ions, and positive ions is created in the drift
space as a result of collisions of electrons with gas molecules during
the drift time of electrons to the anode. The electron transport and
swarm parameters are then determined directly from measurements of the
time-resolved currents of electrons and negative ions arriving at the
anode and of positive ions arriving at the cathode. Resolution of the
arrival spectra of each charged species leads to the most direct inter-
pretation of the measurements and is the approach used in the present
apparatus.

A complete description of the drift tube and of the determina-
tion of swarm parameters from the measured current waveforms together
with their associated measurement uncertainties has already been
documented (Ref. 1) in conjunction with the measurements in dry air.
Paragraphs 2 and 3 describe the additional apparatus and procedures
required for acquiring quantitative data in humid air.

2. IN-SITU MONITORING OF WATER VAPOR CONCENTRATION

The preparation of gas mixtures having accurately known composi-
tion is difficult when a minor constituent of the mixture is a polar
molecule (such as water vapor) because of physical adsorption of the
polar molecule to surfaces within the container. Equilibrium is

5

eventually attained when the adsorption is balanced by desorption and is usually strongly dependent on temperature. In the case of gas mixtures containing water vapor at room temperature, the time to attain equilibrium has been found to be several hours (Ref. 2).

Reproducible gas mixtures containing water vapor have been prepared by first allowing water vapor into the mixing chamber to a known density, freezing out the water vapor in a cold finger, adding the other component gas to a known density, and finally allowing the cold finger to warm up to release the water vapor (Ref. 2). However, there remains some uncertainty concerning the final density of water vapor in the mixture due to possible variations in the adsorption of water vapor to surfaces in the presence of the other components of the mixture. Reproducibility of measured swarm parameters as a function of time following the preparation of the mixture does not ensure that replacement of adsorbed water vapor by other molecules in the mixture has not occurred during mixture preparation.

To remove this ambiguity from the present measurements, a method has been developed for continual in-situ monitoring of the water vapor density in the drift tube prior to, during, and following the preparation of humid air mixtures. The method involves the measurement of the optical absorption produced in a beam of hydrogen Lyman-α radiation traversing a well-defined path in the drift tube volume, the absorption being proportional to the density of water vapor along the path. The choice of the wavelength of the radiation is governed by the requirement that the absorption by water vapor be much larger than that by the other constituents of the mixture. At the wavelength 121.56 nm, corresponding to that of hydrogen Lyman-α, the absorption cross section of water vapor $\sigma(H_2O)$ is (Ref. 3) $1.44 \times 10^{-17} cm^2$ (independent of temperature) whereas that of oxygen $\sigma(O_2)$ is (Ref. 4) $1.23 \times 10^{-20} cm^2$, and nitrogen is transparent. In the present application, the absorption path length is defined by the boundaries of an absorption cell appended to the drift tube envelope.

6

a.   Absorption Cell

A scale drawing of the absorption cell is given in Figure 1
where the numbers refer to the major parts listed in Table 1. The cell
comprises two main subassemblies: (1) the variable length absorption
volume bounded by the concave mirror (item 7) and the vacuum window
(item 31), and (2) the optical component housing (item 20). The entire
assembly is mounted on a 4-1/2 in diameter Conflat flange (item 4) which
is sealed with a metal gasket to a corresponding mating flange (item 4a)
welded in the drift-tube envelope. Figure 2 shows the position of the
absorption region relative to the electron drift region.

The length of the absorption region is variable from 0.1 to 5 cm
by moving the vacuum window axially with respect to the concave mirror.
This is achieved via the vacuum sealing bellows (item 5) which is welded
at one end to the inner circumference of the Conflat flange (item 4) and
at the other end to the outer circumference of a custom vacuum flange
(item 15). The bellows length is controlled by a rotating cylinder
(item 14) threaded internally, where it controls the position of the
threaded mating drive ring (item 8) which is screwed firmly to the
moving vacuum flange (item 15). Rotation of the drive ring (item 8) is
prevented by three guide rods only one of which (item 9) is shown in
Figure 1. Rotation of the drive cylinder (item 14) is possible via the
ballbearing race (item 11) chosen to accept both radial and axial thrust
and for its high precision. The outer ring of this ball race, and the
three guide rods are mounted rigidly on the support flange (item 10)
which is rigidly bolted to the vacuum flange (item 4).

For vacuum processing of the drift tube the optical component
housing is demounted from the vacuum flange (item 15) together with the
bellows drive cylinder, ballbearing race and guide rods (items 14, 11
and 9). To prevent the vacuum window from collapsing under atmospheric
pressure, a bakeout fixture is attached prior to the removal of the
drive cylinder. This fixture consists of four bolts (not shown in
Figure 1) which are fully threaded into four tapped holes in the
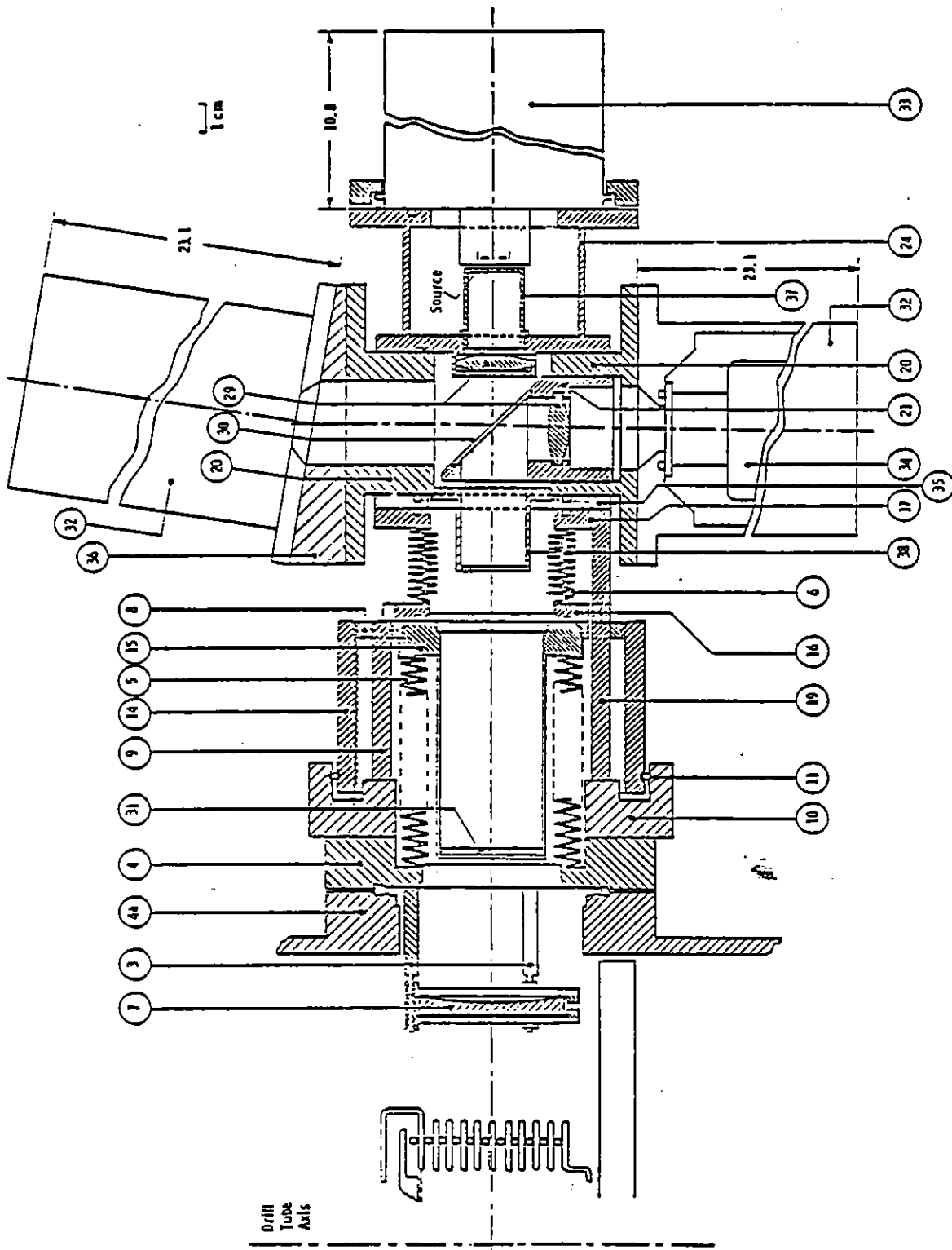
Figure 1. Scale drawing showing the mechanical details of the single-ended optical absorption cell. The numbers used to label the various parts correspond to the part numbers listed in the first column of Table 1.

8

TABLE 1. LIST OF MAJOR PARTS OF OPTICAL ABSORPTION CELL SHOWN IN FIGURE 1

P/N	No. Used	Description		Supplier, P/N
4	1	4-1/2 Conflat Flange	a	954-5079
4a	1	4-1/2 Conflat Flange (Tapped)	a	954-5079
5	1	Welded Stainless Steel Bellows	b	622-60-3
6	1	Welded Stainless Steel Bellows	b	602-55-4
7	1	2" Diam. VUV Mirror 75 mm FL	c	4436/7994
8	1	Threaded Drive Ring		
9	3	1/4" Diam. Guide Rods		
10	1	Support Flange for Drive Mech.		
11	1	Ballbearing Race	d	KA-040-XP3
14	1	Rotating Drive Tube-Internally Threaded		
15	1	Vacuum Flange		
16	1	Gas-tight Flange		
17	1	Gas-tight Flange		
19	3	1/4" Diam. Support Rods		
20	1	Optical Cross Housing		
21	1	Beam Splitter & Lens Holder		
24	1	O_2 Filter and Spacer Tube		
29	2	LiF Biconvex Lens, 25 mm FL	e	
30	1	MgF_2 Beam Splitter 38 mm Diam.	e	
31	1	Tube-mounted MgF_2 Window	e	
32	2	Photomultiplier Housing	f	RFI/B-214 EV
33	1	Lyman-α Source & Exciter	g	399
34	2	Solar-Blind VUV Photomultiplier	f	G26E 314 LF
35	1	Insulating Spacer Flange		
36	1	Wedge Flange		
37	1	Source Aperture		
38	1	Image Aperture		

a) Varian Corporation, Palo Alto, CA
b) Metal Bellows Corporation, Sharon, MA
c) Oriel Corporation, Stamford, CT
d) Keene Corporation, Kaydon Bearing Division, Muskegon, MI
e) Harshaw Chemical Company, Solon, OH
f) EMI Gencom, Plainview, NY
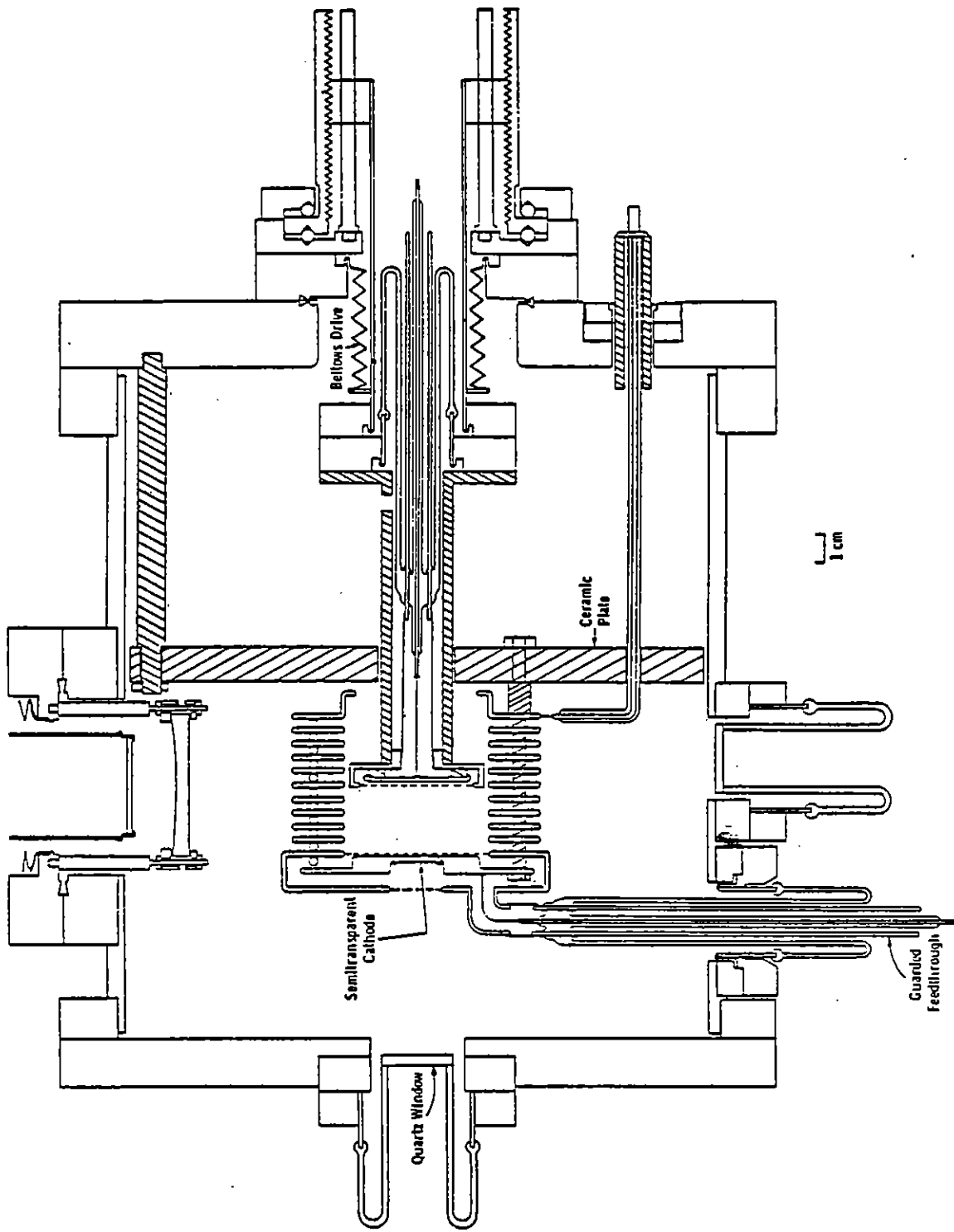g) Quantatec International Inc., Chatsworth, CA

9

Figure 2. Scale drawing showing the location of the absorption region between the mirror and the window at the top of the drawing relative to the electron drift region.

Bellows Drive

Ceramic Plate

Semitransparent Cathode

Guarded Feedthrough

Quartz Window

1 cm

drive ring (item 8) and whose ends bottom on the support flange
(item 10) to maintain a spacing between the retracted window and the
concave mirror. During vacuum processing, the mirror, window, bellows,
drive ring, and support flange (items 7, 31, 5, 8 and 10) are baked at a
temperature of $250^{\circ}C$ along with the remainder of the drift tube and
associated vacuum system.

The optical system used is a dual-beam, single-ended arrangement.
Radiation from a Lyman-α source (item 33) is split into two paths by the
beam splitter (item 30). The light transmitted by the beam splitter is
focussed at the center of curvature of the concave mirror while that
reflected from the front surface of the beam splitter is focussed at the
cathode of one of the photomultiplier tubes (item 34, upper). The light
reflected from the front surface of the beam splitter monitors the
intensity emitted from the source and is used as the reference beam.
The light transmitted through the beam splitter passes through the
vacuum window and is refocussed by the concave mirror at its center of
curvature and thence, after reflection from the back surface of the beam
splitter, at the cathode of the other photomultiplier tube (item 34,
lower). This signal beam passes through the absorption region twice, so
that the absorption path length is equal to twice the separation between
the concave mirror and the vacuum window. The focussing properties of
the system are kept fixed by maintaining a constant separation between
the concave mirror and the remaining optical elements. This is
accomplished by the support rods (item 19) which rigidly attach the
optical cross housing (item 20) to the support flange (item 10). To
accommodate axial motion of the vacuum window within the constraints of
the fixed focus system, a second metal bellows assembly (item 6) is
interposed between the threaded drive ring (item 8) and the optical
cross housing (item 20).

To avoid unwanted absorption at the probing wavelength 121.56
nm, the optical component housing external to the drift tube is made
vacuum tight using O-ring seals wherever appropriate and evacuated to a
pressure $\sim 10^{-6}$ Torr using a separate vacuum system. For operation at

121.56 nm all transmissive optical elements (windows, lenses, beam splitter) are either of LiF or MgF_2. The front surface of the concave mirror is aluminized and overcoated with MgF_2. The beam splitter, which consists of a MgF_2 flat, 38 mm diameter, 1 mm thick, is mounted in a precision machined holder (item 21) which also carries one of the LiF lenses. The mounting angle of 45 deg is fixed in the machining of the holder, but the axial position and rotation of the holder about the axis are both adjustable within the optical cross housing (item 20). This adjustment permits accurate alignment of both beams derived from the beam splitter. The optical cross housing is machined from a solid aluminum block. The flanges which mate with the photomultiplier housings are screwed to the block with countersink screws and a vacuum seal is provided by the incorporation of an O-ring in each joint.

A gas-tight spacer tube (item 24), joined to the optical cross housing with an O-ring seal, couples the Lyman α source (item 33) and houses the source aperture (item 37) and the collimating lens. The 1 mm diameter source aperture provides desirable point-source optical geometry and allows the use of focal plane apertures for discriminating against scattered light. The main sources of scattered light in the signal beam channel have been identified as reflected light from the vacuum window (item 31) and from the entrance window of the photomultiplier which monitors the reference beam intensity.[*] Scattered light from the vacuum window is reduced considerably by the 4 mm diameter aperture (item 38) placed in the focal plane of the collimating lens and coincidently of the concave mirror. Contributions to the signal beam intensity from light reflected by the reference beam photomultiplier window is reduced

---

[*]Reflection also occurs from the entrance window of the photomultiplier which monitors the signal beam intensity, and reflected light from this source contributes to the reference beam signal. However, in the present system, this contribution is less than 1% of the true reference beam intensity even with no absorption in the drift tube, i.e., with maximum signal beam intensity. Consequently, no attempt has been made to reduce this scattered light component, for example, by tilting the signal beam photomultiplier.

by tilting the photomultiplier window sufficiently that the reflected light is outside the acceptance angle of the signal beam photomultiplier. This is accomplished by the wedge spacer flange (item 36) interposed between the optical cross housing (item 20) and the photomultiplier housing (item 32, upper). Both photomultiplier housings are joined to the optical cross housing with O-ring seals. In addition an O-ring seal between the entrance window of each photomultiplier and the internal surface of its housing flange preserves the vacuum integrity of the optical component housing.

The electronic circuitry associated with the absorption cell system utilizes photon counting and is illustrated schematically in Figure 3. The output from each photomultiplier is fed through an amplifier (LeCroy Model VV100B) having a voltage gain of 10 and a band width of 230 MHz to a discriminator (LeCroy Model LD 601C) having a pulse-pair resolution of 9 ns followed by a 320 MHz decade prescaler (Fairchild Model 95H90) and then to one channel of a dual-channel counter. The counter is arranged so that both channels remain active until a predetermined number of counts have been accumulated in the reference channel B at which time the counter is stopped and the contents of both channels read. The use of a wide bandwidth system enables a statistical variation in the transmitted count of ~ 1 part in 10^4 to be obtained with a counting time of ~ 10 s. To prevent electrical ground loops between the absorption cell readout circuitry and the waveform recording circuitry from the drift tube an insulating spacer flange (item 35 in Figure 1) is inserted between the optical cross housing (item 20 in Figure 1) and the bellows flange (item 17 in Figure 1).

The light source (item 33 in Figure 1) is an rf-excited hydrogen discharge lamp which emits a multiline spectrum together with an extensive continuum. Two filters are used to isolate the Lyman-α line from the remaining spectrum. First, the photomultiplier detectors used are of the solar-blind type and are sensitive only over the range from 110 nm (the MgF_2 entrance window cut-off) to 200 nm. These provide
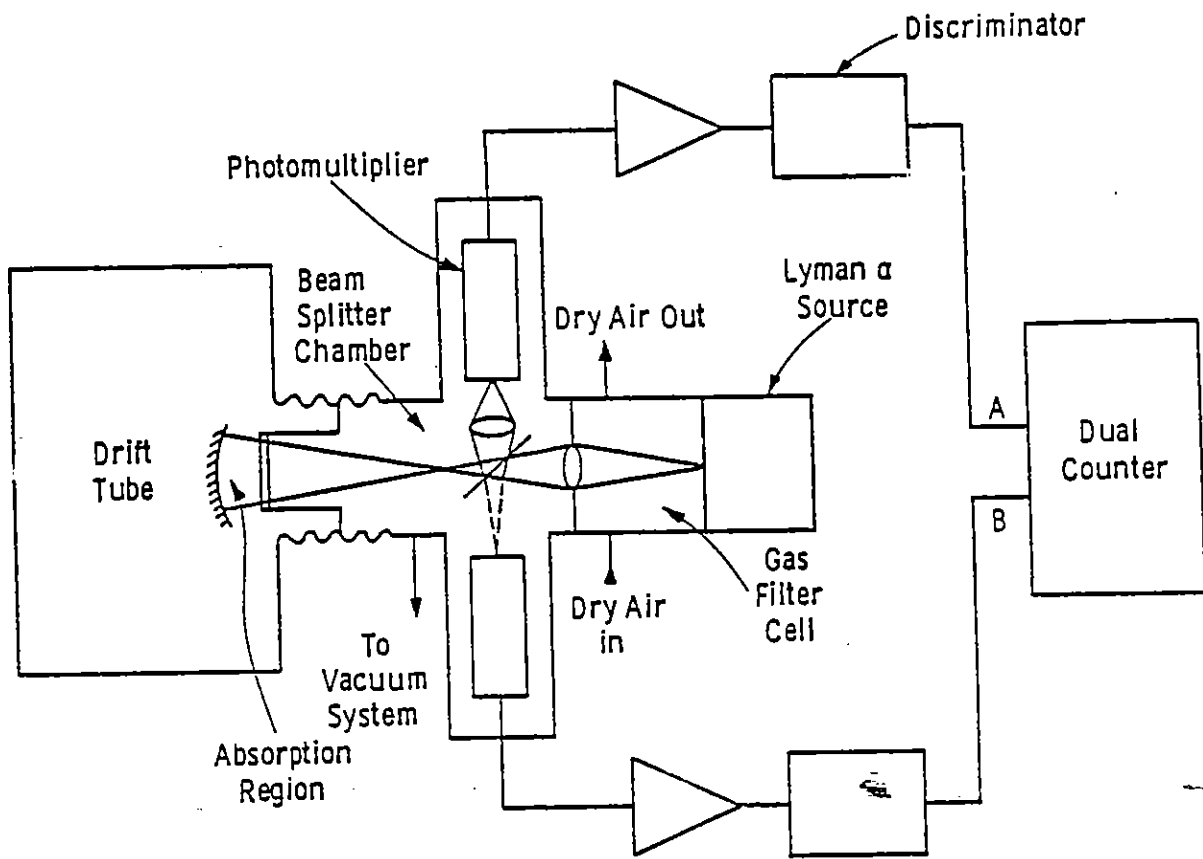
Figure 3. Schematic drawing of the optical absorption monitoring system.

broadband filters which eliminate radiation of wavelengths longer than 200 nm. Within the sensitive range, a narrow band filter transmitting at the Lyman-α wavelength is provided by allowing the light from the source to pass through an appropriate optical path length in oxygen. The gas-tight spacer tube (item 24) is used for the oxygen absorption filter cell. For convenience, dry air is substituted for pure oxygen in the filter cell using an arrangement in which the cell is continuously flushed at atmospheric pressure. The excellent discrimination provided by this filter combination is illustrated in Figures 4 and 5. Figure 4 shows the spectrum emitted from the source detected by the solar-blind photomultiplier, i.e., after passage through the broad band filter. This spectrum was recorded using a vacuum monochromator with a spectral resolution of 0.3 nm. To accommodate the more intense Lyman-α line, the photomultiplier current sensitivity in the immediate wavelength vicinity of Lyman-α has been reduced by a factor of 10. Figure 5 shows the spectrum recorded by the photomultiplier under identical conditions except that the light from the source is allowed to pass through a dry air filter interposed between the source and the entrance slit of the monochromator and having the same optical density as the filter cell in Figure 1 (item 24). Comparing the spectrum of Figure 5 with that of Figure 4 it is seen that while the intensity of the Lyman-α line is reduced by only ~ 40% the remaining unwanted spectrum is reduced to the dark current level of the photomultiplier. Thus, in this wavelength range the oxygen filter provides a much narrower bandwidth filter than is available, for example, from a dielectric filter.

The modular design of the absorption cell system enables the complete optical alignment of the system to be carried out before attachment to the drift tube. The initial alignment is carried out using the light emitted from the source which lies in the visible region of the spectrum. During this stage the LiF lenses are replaced by glass lenses whose focal length in the visible matches that of the LiF lenses at 121.56 nm. The relative position of the beam splitter is adjusted so that both derived beams are optically centered and the axial position of
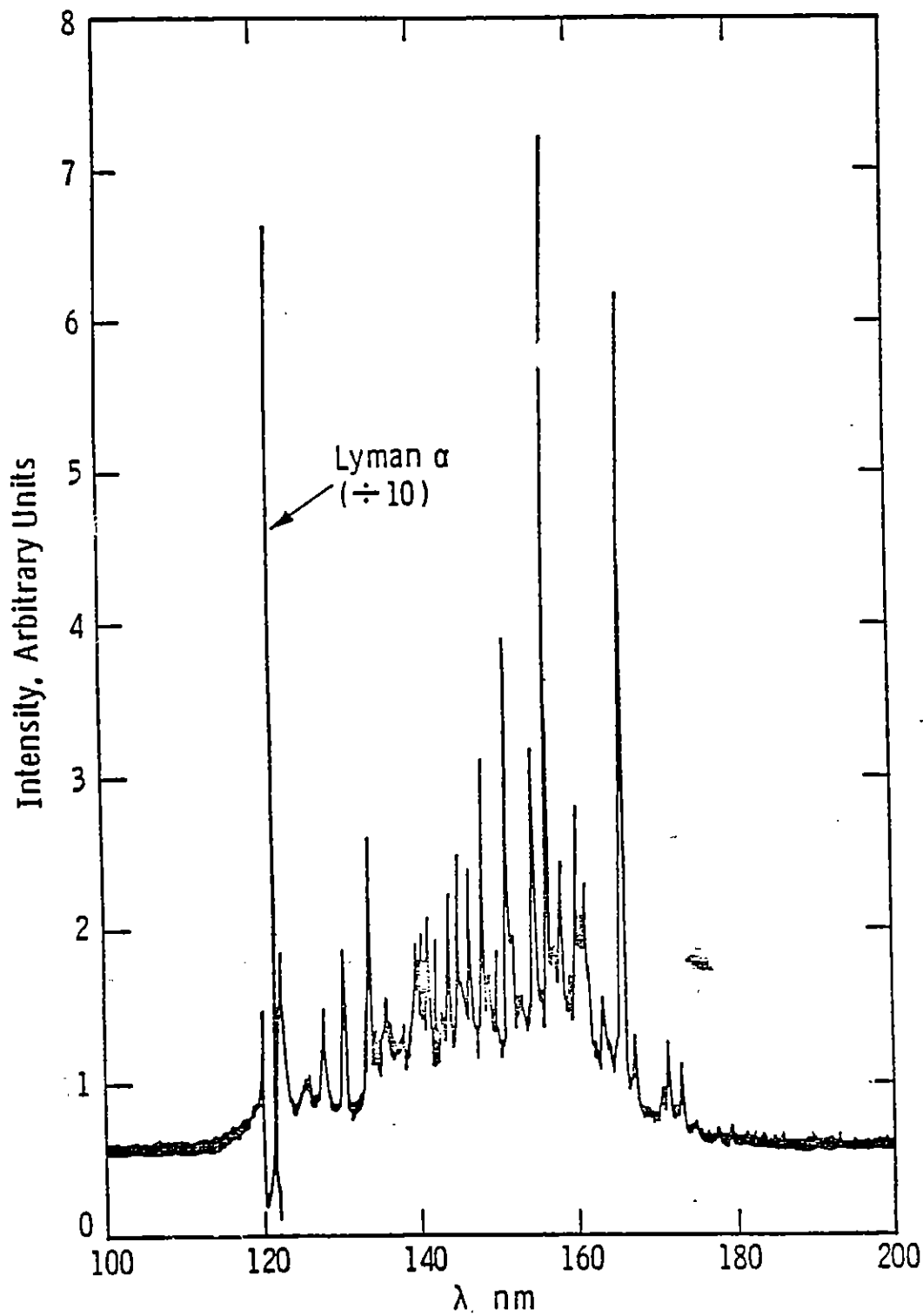
Figure 4. Total spectrum emitted from the Lyman-α source in the wavelength range from 110 to 200 nm. The sensitivity in the region of the Lyman-α peak is reduced by a factor of ten compared with the remainder of the scan.
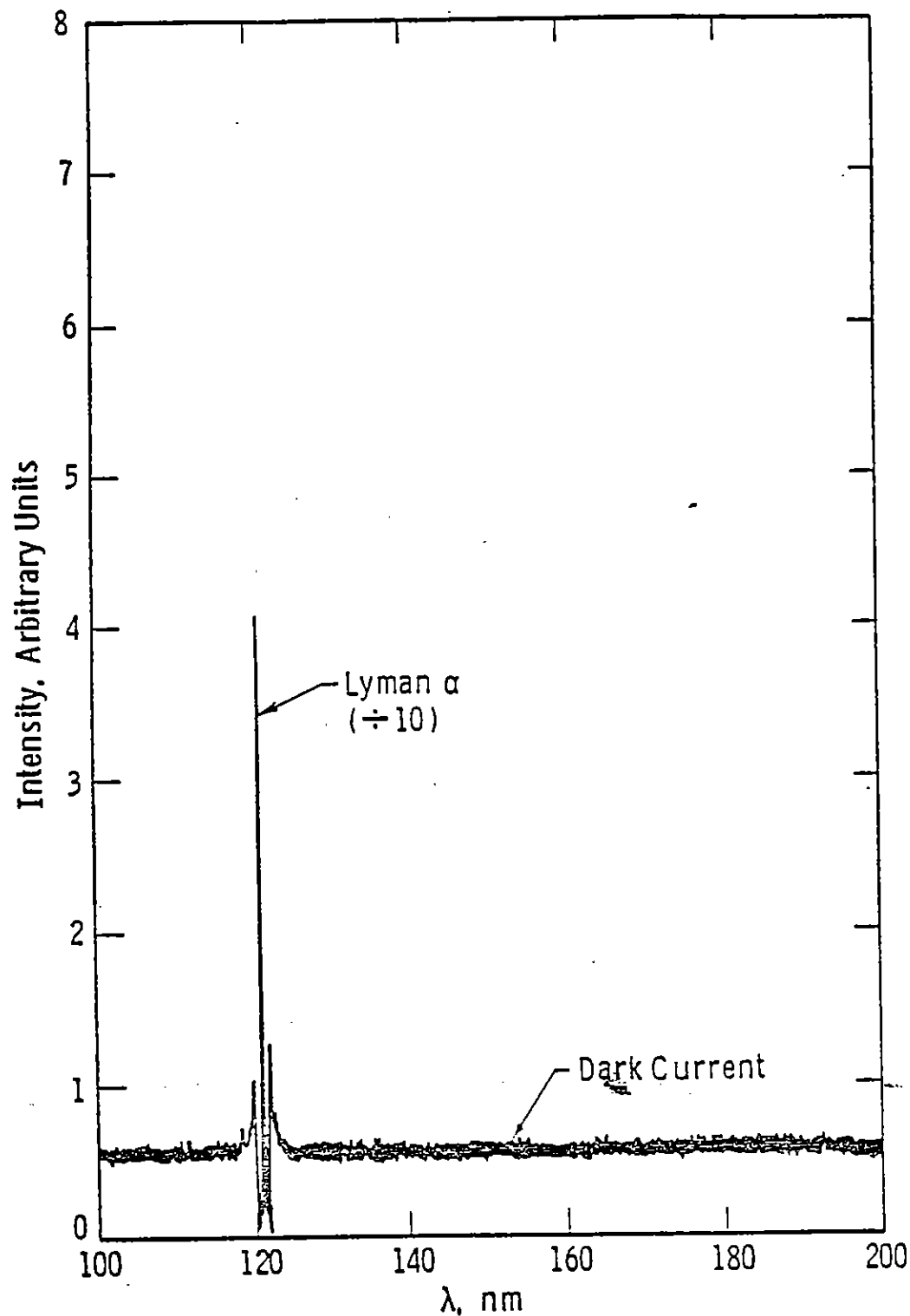
Figure 5. Spectrum recorded under identical conditions to Figure 4 with the exception that a dry air filter is interposed between the source and the detector. The sensitivity in the region of the Lyman-α peak is again reduced by a factor of ten. The remainder of the scan represents the photomultiplier dark current.

the image aperture adjusted to be in the focal plane of the collimating lens. In the final alignment stage (with the LiF lenses installed) the intensity of the signal beam at 121.56 nm is optimized by adjusting the lateral position of the source with respect to the optic axis of the cell defined by the source aperture.

The variable absorption path length allows differential measurements to be made thereby eliminating end effects and errors associated with condensation of water vapor on the vacuum window and concave mirror. In addition, by making differential measurements, the true component (i.e., that component which has passed through the absorption region) of the total signal detected by the signal beam photomultiplier may be separated from the unwanted component due to light scattered into the detector from surfaces within the optical component housing as discussed in more detail in paragraph 2b.

b. Calibration of Absorption Cell

For a beam of radiation of a particular wavelength traversing an optical path ℓ through an absorbing gas mixture of total density N, the transmission T is given by

$$T = \exp \left(- \ell \sum_i \sigma_i N_i \right) \qquad (1)$$

where σ_i and N_i are the absorption cross section and density, respectively, of the ith component species of the mixture and $N = \sum_i N_i$. In the present application of absorption of Lyman-α radiation by humid air, the absorbing species are H_2O and O_2 and Equation (1) may be written in the form

$$T = \exp \left\{-N\ell \left[f'(1-f)\sigma(O_2)+ f\sigma (H_2/0) \right] \right\} \qquad (2)$$

where f is the fractional density of water vapor in the mixture and f' is the fractional density of oxygen in dry air, i.e., $f = [H_2O]/N$ and $f' = [O_2]/[Dry \ Air]$.

18

Despite precautions taken to reduce the contribution of the measured signal due to scattered light, it still remains a substantial fraction (~ 40%) of the total signal. However, the true signal component which has passed through the absorption region may be extracted from the total signal by making differential measurements. If $I(\ell)$ is the total intensity of the signal beam detected for an absorption path ℓ, then

$$I(\ell) = I_1 + I_2 \exp (- A N \ell) \qquad (3)$$

where I_1 is the intensity contribution due to scattered light, I_2 is the intensity of the light incident on the absorption region in the drift tube, and A is given [from Equation (2)] by

$$A = f' (1-f) \sigma(O_2) + f\sigma(H_2O) \qquad (4)$$

Equation (3) may be rewritten in the form

$$I(\ell) = I(\ell+\Delta\ell) \exp (AN\Delta\ell) - I_1 [\exp (AN\Delta\ell)-1] \qquad (5)$$

Thus, by making measurements of the total intensity of the signal beam for a sequence of absorption path lengths differing by a constant increment $\Delta\ell$, a plot of $I(\ell)$ versus $I(\ell+\Delta\ell)$ is linear of slope S given by

$$S = \exp \{N\Delta\ell[f'(1-f)\sigma(O_2) + f\sigma(H_2O)]\} \qquad (6)$$

Therefore, provided the absorption cross sections are known, the fractional concentration f is determined from

$$f = \ell nS/\{N\Delta\ell[\sigma(H_2O)-f'\sigma(O_2)\} - f'\sigma(O_2)/[\sigma(H_2O)-f'\sigma(O_2)] \qquad (7)$$

Using published values of the cross sections (Refs. 3, 4) and a value of $f' = 0.209$, corresponding to the value pertaining to the dry air used in the present study (Ref. 1), it is seen that the ratio of the first to second terms in Equation (2) is less than 1% for values of $f = 0.0175$. Thus, for the present application in humid air for $f = 0.02$, Equations (2), (6) and (7) may be replaced with

$$T = \exp\left[-N\ell f\sigma(H_2O)\right] \qquad (8)$$

$$S = \exp\left[N\Delta\ell f\sigma(H_2O)\right] \qquad (9)$$

$$f = \ell nS/[N\Delta\ell\sigma(H_2O)] \qquad (10)$$

Calibration of the present absorption cell is carried out with the cell attached to the drift tube. The procedure consists of introducing a known density of pure water vapor into the drift tube, determined using the Baratron gauge appended to the system (Ref. 1), and measuring the intensity of Lyman-α radiation transmitted through the absorption cell as a function of the length of the absorption path. Typical measurements are shown by the solid points in Figure 6 where the intensity $I(\ell)$ is plotted as a function of $I(\ell+\Delta\ell)$ for a constant path increment $\Delta\ell = 0.8$ cm and a density of water vapor $N(H_2O) = 1.421 \times 10^{22}$ m^{-3}. The slope of the plot determined by linear regression analysis (as indicated by the solid line in Figure 6) gives the value of $\sigma(H_2O)$ from Equation (8). From a series of similar measurements taken at different densities of pure water vapor, the cross section $\sigma(H_2O)$ has been determined to be $(1.42 \pm 0.3) \times 10^{-17}$ cm^2, in very good agreement with the value 1.44×10^{-17} cm^2 obtained in previous measurements (Ref. 3). Using this value of $\sigma(H_2O)$ the fractional concentration of water vapor in the humid air mixture is then determined from Equation (10).

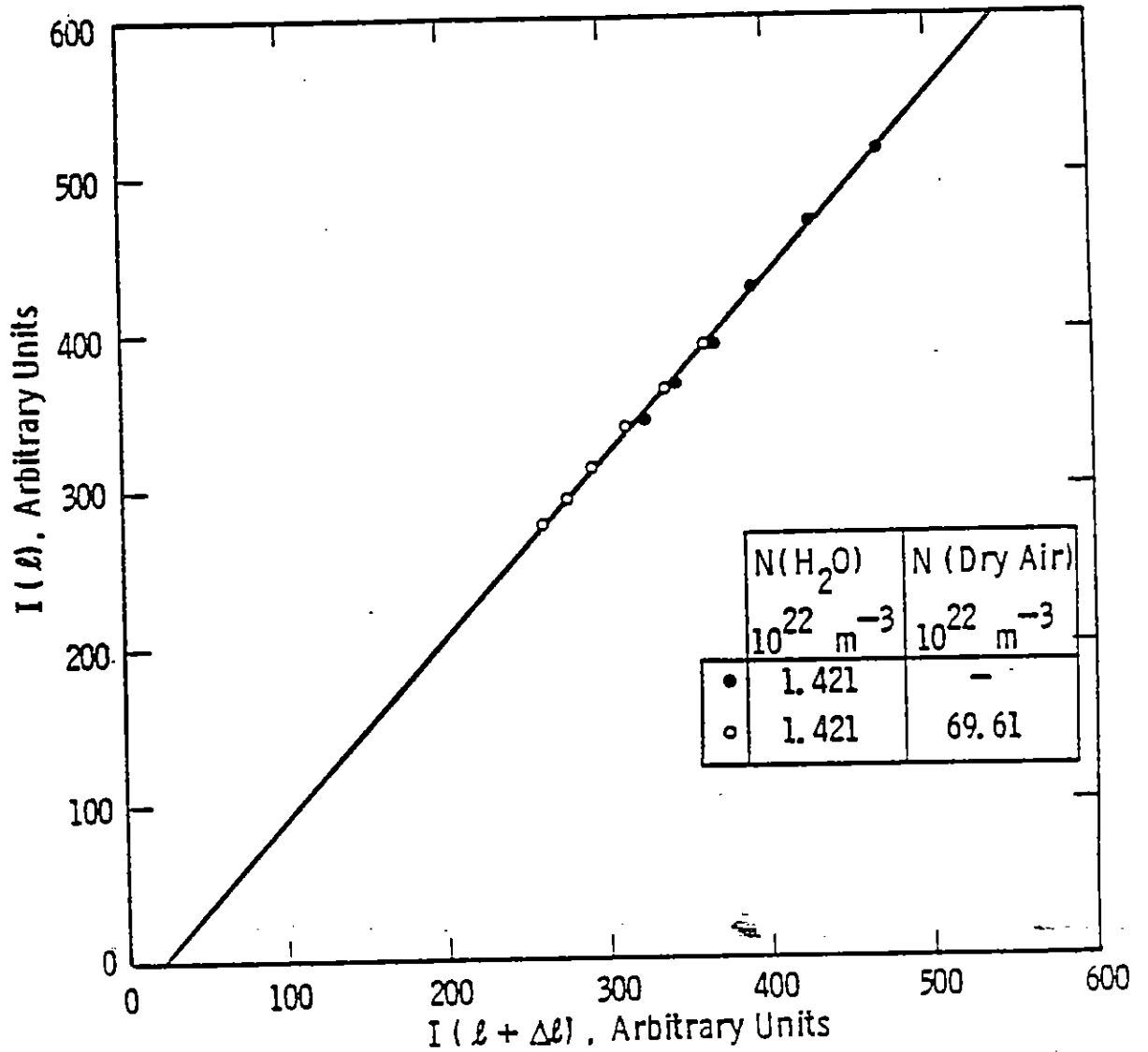Figure 6. Plot of the intensity of the Lyman-α signal measured for an absorption path ℓ versus that measured for a path ℓ + Δℓ. The solid points correspond to measurements in pure water vapor and the open points to measurements in humid air (2.00% H_2O).

3. PREPARATION OF DRY AIR-WATER VAPOR MIXTURES

The gas-handling and vacuum systems associated with the drift tube facility are shown schematically in Figure 7. The dry air and water vapor supplies are connected to the gas manifold through separate valves. To prepare a humid air mixture, the minor component, i.e., water vapor, is first admitted to the preevacuated drift tube to a given pressure and the drift tube isolating valve closed. The water vapor pressure, as measured with the Baratron gauge and monitored with the optical absorption system, decreases initially with time due to adsorption on the internal surfaces of the drift tube. After a period ~ 48 h, the pressure finally equilibrates at a value p_w, during which time a quantity of ~ 10 Torr-ℓ of water vapor is adsorbed within the drift tube. The gas manifold is then reevacuated to a pressure ~ 10^{-6} Torr[*] and pressurized with dry air. Dry air is bled into the drift tube through the isolating valve to a total pressure p_T given by p_w/f, where f is the desired fractional concentration of water vapor in the mixture.

After preparation of the mixture, the water vapor concentration is monitored using the absorption cell. Some typical measurements are shown by the open points in Figure 6. These denote the intensity $I(\ell)$ plotted versus $I(\ell+\Delta\ell)$ for a constant path increment $\Delta\ell = 0.8$ cm and a humid air mixture of total density $N = 71.0 \times 10^{22}$ m^{-3} formed by adding dry air to a water vapor sample of density $N(H_2O) = 1.421 \times 10^{22}$ m^{-3}, i.e., f = 0.0200. Comparison of the data (solid points) taken before the addition of dry air with the measurements (open points) recorded after mixture preparation shows that, to within the experimental uncertainty, the density of water vapor has remained unchanged. This behavior has been found for all mixtures prepared in the present study.

---

[*]The residual pressure in the vacuum and gas-handling systems following bakeout of the entire system is in the low 10^{-9} Torr range. However, following exposure of the system to water vapor, the base vacuum pressure attainable without rebaking the system is ~ 10^{-6} Torr due to slow desorption of water vapor from internal surfaces.
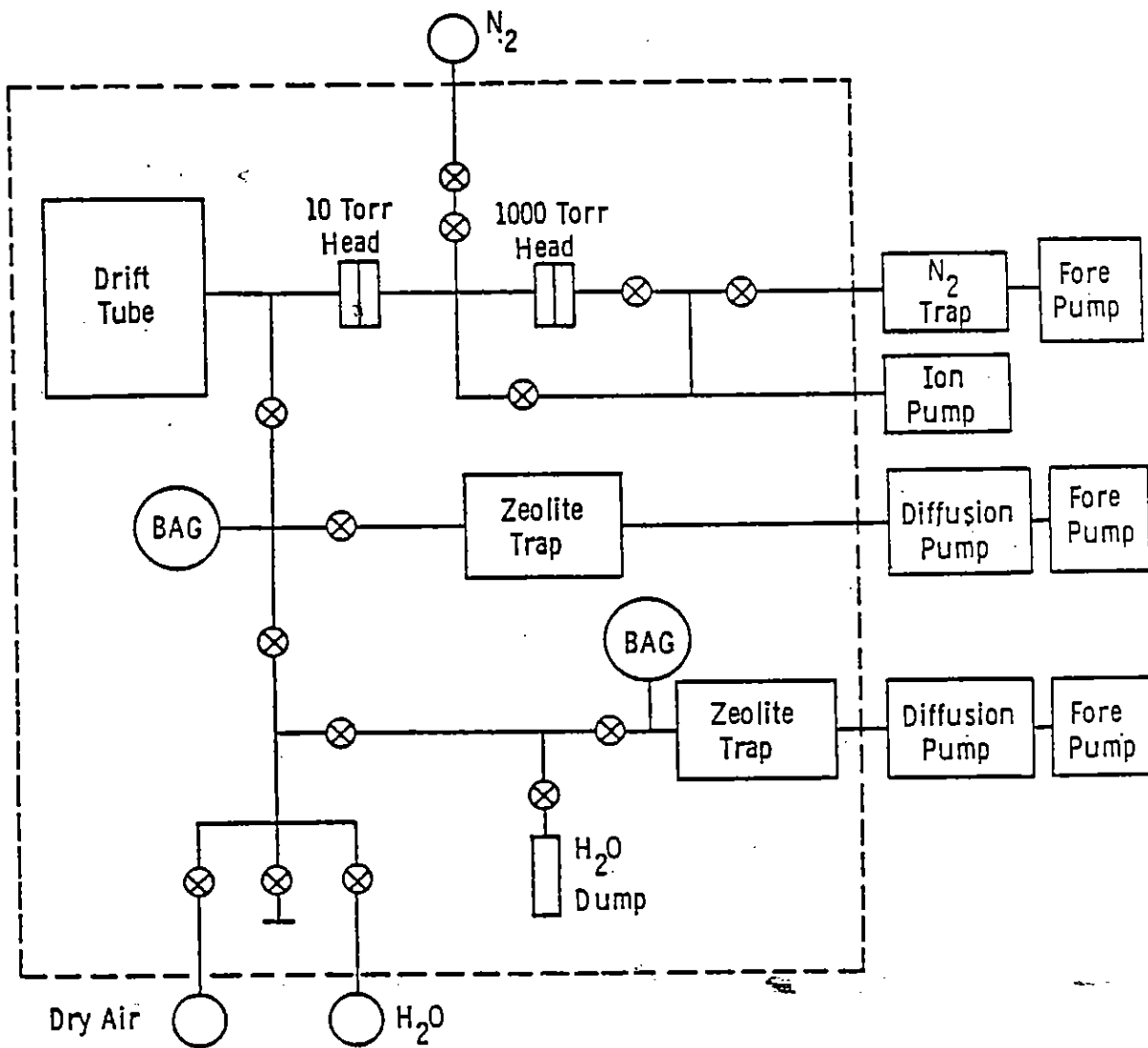
Figure 7. Schematic drawing of the vacuum and gas-handling system used for the preparation of the humid-air samples. The dashed rectangle encloses that portion of the system subjected to bakeout.

Moreover, subsequent periodic absorption measurements have ensured that the mixture composition remains unchanged during measurements of swarm parameters in a given gas mixture sample.

The uncertainty in the determination of the fractional concentration of water vapor from the optical absorption measurements is estimated to be ± 2%. The absorption system in its present form may be used for the determination of f over the entire range, from 0.005 to 0.04, of interest for the measurement and swarm parameters in humid air.

III. RESULTS FOR HUMID AIR (2% H_2O)

The present measurements have been carried out in humid air mixtures with $f = 0.0200$. The dry air component, supplied by Matheson Co. is obtained from the same cylinder used for the measurements in dry air and an analysis of the composition has been given previously (Ref. 1). The water sample was prepared, using a separate ultrahigh vacuum system, by vacuum distillation of distilled water into a prebaked container equipped with an isolation valve. To minimize the transfer of impurities, the distillation was carried out near room temperature and only half the original volume was transferred into the container. As a further check on the purity of the water vapor sample, measurements of electron drift velocity in water vapor have been carried out over the range of E/N from 10 to 50 $\times 10^{-21}$ V·m^2. The present measurements are in excellent agreement, to within the combined experimental uncertainties, with the currently accepted values (Refs. 5, 6).

1. ELECTRON MOBILITY

A summary of the values of w_e and the derived reduced mobility μ_e as a function of E/N is given in Figure 8 and in Table 2. The upper abscissa scales in Figure 8 (along with the subsequent figures) show the corresponding values of electric field at atmospheric density for three different altitudes, 0 km, 15 km, and 30 km. The data cover the range of E/N from 6×10^{-22} to 3×10^{-19} V·m^2. The uncertainty in the values of w_e and μ_e is estimated to be ± 1% for values of E/N in the range $10^{-20} < E/N < 10^{-19}$ V·m^2 and ± 2% for E/N < 10^{-20} V·m^2 and E/N > 10^{-19} V·m^2. No corrections have been applied to the data for attachment or ionization effects; based on available knowledge such corrections are estimated to be less than the assigned uncertainty.
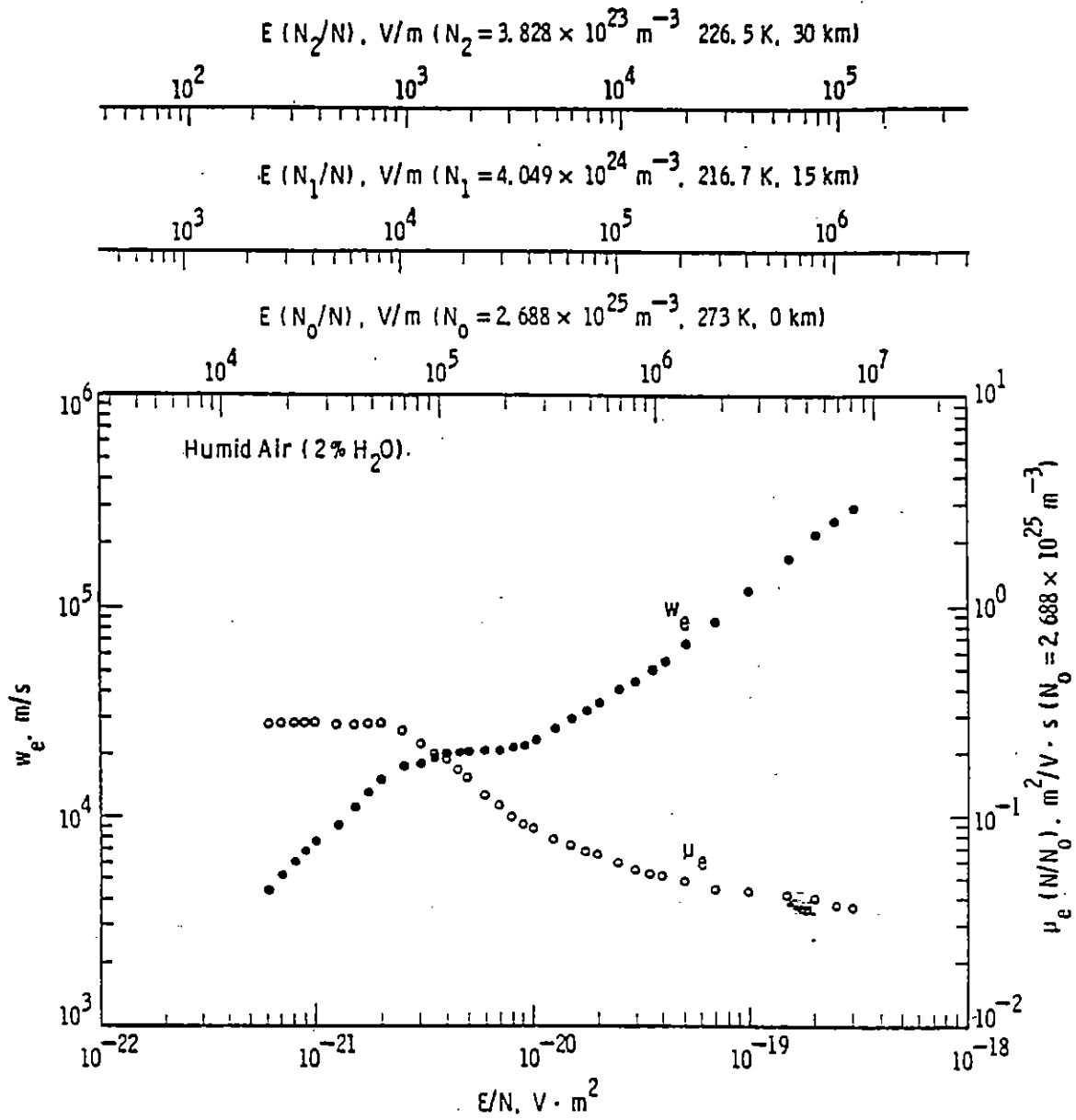
Figure 8.   Summary of the present measurements of electron drift velocity
or electron mobility as a function of E/N.

E/N 10^{-21} V·m²	E N_0/N 10^4 V/m	f(H_2O) = 0		f(H_2O) = 0.0200	
		$\mu_e N$ 10^{24}/V·m·s	$\mu_e N/N_0$ m²/V·s	$\mu_e N$ 10^{24}/V·m·s	$\mu_e N/N_0$ m²/V·s
0.600	1.613	8.25	0.307	7.43	0.277
0.700	1.882	7.59	0.282	7.47	0.278
0.800	2.150	7.10	0.264	7.49	0.279
0.900	2.419	6.78	0.252	7.56	0.281
1.000	2.688	6.58	0.245	7.58	0.282
1.250	3.360	6.04	0.225	7.41	0.276
1.500	4.03	5.39	0.201	7.40	0.275
1.750	4.70	5.09	0.189	7.49	0.279
2.000	5.38	4.77	0.177	7.38	0.275
2.500	6.72	4.16	0.155	6.98	0.260
3.000	8.06	3.73	0.139	5.97	0.222
3.500	9.41	3.40	0.127	5.49	0.204
4.00	10.75	3.18	0.118	5.05	0.188
4.50	12.10	2.96	0.110	4.51	0.168
5.00	13.44	2.82	0.105	4.11	0.153
6.00	16.13	2.58	0.0961	3.42	0.127
7.00	18.82	2.39	0.0887	3.01	0.112
8.00	21.50	2.24	0.0832	2.70	0.100
9.00	24.19	2.12	0.0789	2.49	0.0926
10.00	26.88	2.09	0.0777	2.36	0.0878
12.50	33.60	1.94	.0723	2.10	0.0780
15.00	40.3	1.80	.0670	1.96	0.0729
17.50	47.0	1.71	.0638	1.84	0.0685
20.00	53.8	1.64	.0610	1.78	0.0662
25.00	67.2	1.56	0.0582	1.62	0.0601
30.00	80.6	1.49	0.0556	1.48	0.0549
35.00	94.1	1.43	0.0530	1.43	0.0531
40.0	107.5	1.40	0.0519	1.39	0.0518
45.0	121.0	1.36	0.0504		
50.0	134.4	1.33	0.0496	1.33	0.0496
60.0	161.3	1.24	0.0461		
70.0	188.2	1.21	0.0449	1.21	0.0451
80.0	215.0	1.20	0.0446		
90.0	241.9	1.21	0.0451		
100.0	268.8	1.21	0.0450	1.19	0.0443
125.0	336.0	1.17	0.0434		
150.0	403	1.12	0.0417	1.13	0.0419
175.0	470	1.12	0.0417		
200.0	538	1.10	0.0407	1.09	0.0407
250.0	672	1.01	0.0375	1.02	0.0378
300.0	806	0.98	0.0366	0.98	0.0365

$N_0 = 2.688 \times 10^{25} m^{-3}$

Estimated uncertainties in the measured quantities are:

E/N: $\pm$ 0.2%; f: $\pm$ 2%

$\mu_e N$, $\mu_e N/N_0$ (f = 0): $\pm$ 1% for E/N $\leq$ 10^{-19} V·m²; $\pm$ 2% for E/N > 10^{-19} V·m²

$\mu_e N$, $\mu_e N/N_0$ (f = 0.0200): $\pm$ 1% for $10^{-20} \leq$ E/N $\leq$ 10^{-19} V·m²; $\pm$ 2% for
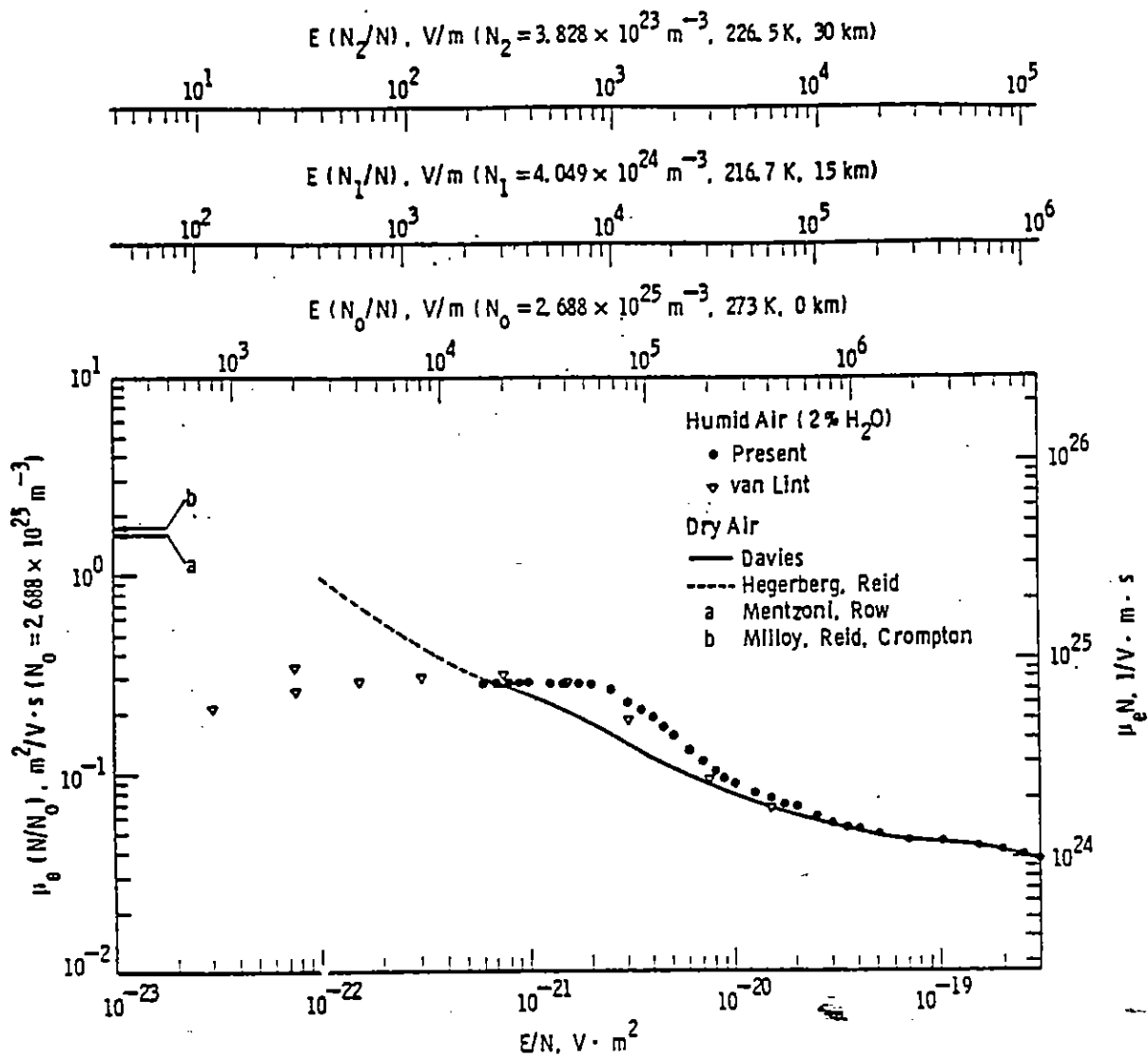E/N < 10^{-20} V·m² and E/N > 10^{-19} V·m²

Figure 9. Comparison of the present measurements of electron mobility with previous data in humid air containing the same water vapor concentration. The dashed and solid lines correspond to previous measurements in dry air. The arrows on the ordinate correspond to determinations of the mobility of thermal electrons in dry air.

A comparison of the present values of electron mobility with previous data in humid air for $f = 0.02$ (Ref. 7) and in dry air (Refs. 1, 8) is presented in Figure 9. For the sake of clarity the data in dry air are denoted by a smooth curve drawn through the experimental points. The left ordinate scale represents the value of reduced mobility μ_e while the right ordinate corresponds to the mobility at a density $N_o = 2.688 \times 10^{25}$ m^{-3}. Also indicated in Figure 9 (by the arrows on the left ordinate) are the values of the mobility of thermal electrons in dry air, 1.59 m^2/V·s deduced from the measurements of electron collision frequencies in oxygen (Ref. 9) and nitrogen (Ref. 10), and 1.75 m^2/V·s deduced from measurements of electron mobility in dry air-carbon dioxide mixtures (Ref. 11).

The data obtained in the present study are the first comprehensive set of measurements in humid air over an extended range of E/N. For values of E/N $\leq 2 \times 10^{-21}$ V·m^2, the electron mobility is found to be constant with a mean value of 0.278 ± 0.006 m^2/V·s and corresponds to the mobility of thermal electrons. This value is in very good agreement with that, 0.271 ± 0.016 m^2/V·s, determined by van Lint (Ref. 7). For values of E/N $> 3 \times 10^{-20}$ V·m^2, the data agree, within experimental error (± 2%), with the previous measurements in dry air. In the intermediate range of E/N, the values of van Lint (Ref. 7) are up to 20% lower than the present results.

As may be seen from Figure 9, the effect of water vapor on the electron mobility in air is most pronounced at low values of E/N where the large momentum transfer cross section in water vapor dominates despite the low concentration of water vapor in the mixture. The major contribution to the momentum transfer cross section at very low electron mean energies is expected to be from rotational excitation.

2. NEGATIVE ION MOBILITIES

A summary of the values of the reduced negative-ion mobility, which have an estimated uncertainty of ± 1%, is given in Table 3 and

Figure 10 where the values are compared with previous data for dry air (Ref. 1). As in the case of dry air, the negative-ion waveforms show the presence of only one dominant ion. However, based on the widely different mobilities, the identity of the ions for values of $E/N < 4 \times 10^{-20}$ V$\cdot$m^2 is probably different from that for $E/N > 6 \times 10^{-20}$ V$\cdot$m^2 and the dashed line in Table 3 indicates this distinction.

Over the range of E/N from 6×10^{-22} to 4×10^{-20} V$\cdot$m^2, the values of the mobility are constant, having a mean value of $(1.86 \pm 0.02) \times 10^{-4}$ m^2/V$\cdot$s. This suggests that over this range of E/N, the observed ions are in thermal equilibrium with the gas. The lower value found for the mobility in humid air compared with that in dry air indicates that the dominant ion in humid air has a different identity than that in dry air. In this region of E/N, previous work (Ref. 12) has shown that the primary ion is O_2^- formed in the three-body reaction

$$e + O_2 + M \rightarrow O_2^- + M \tag{11}$$

where the third body M is either an oxygen, nitrogen, or water vapor molecule. Among the possible reactions of the O_2^- ions which can occur are

$$O_2^- + O_2 + M \rightarrow O_4^- + M \tag{12}$$

$$O_2^- + CO_2 + M \rightarrow CO_4^- + M \tag{13}$$

$$O_4^- + CO_2 \rightarrow CO_4^- + O_2 \tag{14}$$

$$O_2^- + H_2O + M \rightarrow O_2^- \cdot H_2O + M \tag{15}$$

$$O_2^- \cdot H_2O + H_2O + M \rightarrow O_2^- (H_2O)_2 + M \tag{16}$$

$$O_2^- \cdot H_2O + CO_2 \rightarrow CO_4^- + H_2O \tag{17}$$
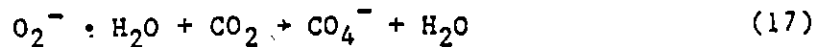
TABLE 3. VALUES OF THE NEGATIVE-ION MOBILITY IN HUMID AIR (2.00% H_2O)
COMPARED WITH PREVIOUS MEASUREMENTS (REF. 1) IN DRY AIR

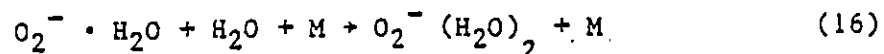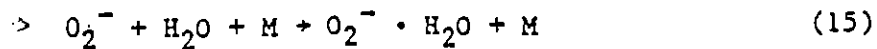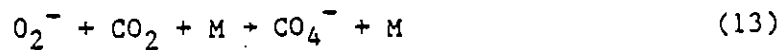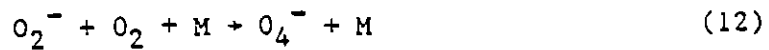| E/N | EN_o/N | $f(H_2O) = 0$ | | $f(H_2O) = 0.0200$ | |
| | | $\mu_- N$ | $\mu_- N/N_o$ | $\mu_- N$ | $\mu_- N/N_o$ |
10^{-21}V·m^2	10^4V/m	10^{21}/V·m·s	10^{-4}m^2/V·s	10^{21}/V·m·s	10^{-4}m^2/V·s
0.600	1.613	6.13	2.28	4.97	1.85
0.800	2.150	6.11	2.27	4.96	1.85
1.000	2.688	6.12	2.28	5.01	1.86
1.500	4.03	6.09	2.27	4.99	1.86
2.000	5.38	6.12	2.28	4.97	1.85
3.000	8.06	6.09	2.27	5.00	1.86
4.00	10.75	6.11	2.27	4.96	1.85
5.00	13.44	6.09	2.26	4.98	1.85
6.00	16.13	6.11	2.27	4.97	1.85
7.00	18.82	6.12	2.28	4.96	1.85
8.00	21.50	6.14	2.28	4.98	1.85
9.00	24.19	6.13	2.28	5.00	1.86
10.00	26.88	6.13	2.28	4.99	1.86
12.50	33.60	6.10	2.27	5.00	1.86
15.00	40.3	6.10	2.27	5.01	1.86
17.50	47.0	6.10	2.27	5.03	1.87
20.00	53.8	6.13	2.28	5.00	1.86
25.00	67.2	6.10	2.27	5.00	1.86
30.00	80.6	6.13	2.28	5.03	1.87
35.00	94.1	6.10	2.27	4.97	1.85
40.00	107.5	6.10	2.27	5.00	1.86
60.0	161.3	8.14	3.03	6.64	2.47
70.0	188.2	8.47	3.15	6.91	2.57
80.0	215.0	8.66	3.22	7.10	2.64
90.0	241.9	8.84	3.29	7.20	2.68
112.5	302.4	8.79	3.27	7.39	2.75
125.0	336.0	8.55	3.18	7.47	2.78
137.5	369.6	8.23	3.06	7.50	2.79
150.0	403	8.00	2.98	7.53	2.80
175.0	470	7.66	2.85	7.50	2.79
200.0	538			7.39	2.75
225.0	605			7.12	2.65

$N_o = 2.688 \times 10^{25}$m^{-3}

Estimated uncertainties in the measured quantities are:

E/N: $\pm$ 0.2%; f: $\pm$ 2%

$\mu_- N$, $\mu_- N/N_o$ (f = 0): $\pm$ 1%
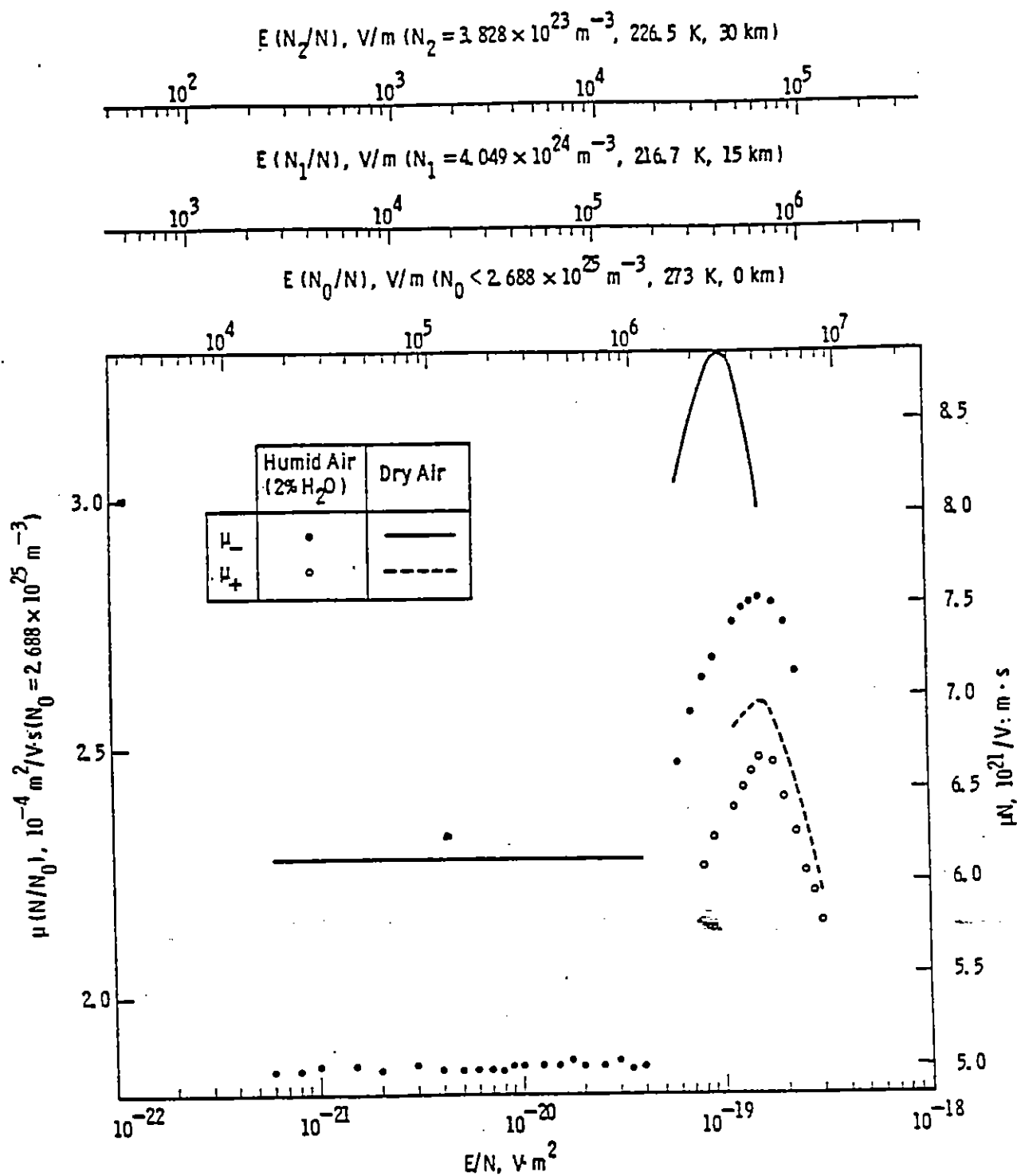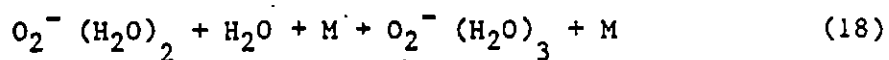
$\mu_- N$, $\mu_- N/N_o$ (f = 0.0200): $\pm$ 1%

Figure 10. Summary of the present measurements of negative-ion (solid points) and positive-ion mobility (open points) as a function of E/N compared to previous measurements in dry air (solid and dashed curves, respectively).
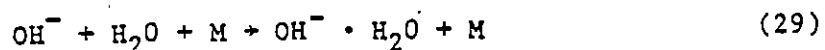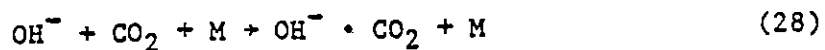
$$O_2^- (H_2O)_2 + H_2O + M \rightarrow O_2^- (H_2O)_3 + M \qquad (18)$$

Studies of these reactions have been made with O_2 as the third body (i.e., $M=O_2$). From these studies, the first six reactions have thermal rate coefficients of 3.0×10^{-43} m^6/s, 4.7×10^{-41} m^6/s, 4.3×10^{-16} m^3/s, 2.2×10^{-40} m^6/s, 6×10^{-40} m^6/s, and 5.8×10^{-16} m^3/s, respectively (Refs. 13-16), while the last reaction has an equilibrium constant of 8.2×10^3 atm^{-1} (Ref. 14). Assuming that the same values apply with N_2 as the third body (i.e., $M = N_2$), then for the densities of N_2 ($> 2.3 \times 10^{24} m^{-3}$), O_2 ($> 6.3 \times 10^{23} m^{-3}$), CO_2 ($< 3.6 \times 10^{19} m^{-3}$), and H_2O ($> 6 \times 10^{22}$ m^{-3}) pertaining to the air mixtures used in the present study, the dominant reaction path of the O_2^- ions is expected to lead to the formation of $O_2^- (H_2O)_2$ via the reactions described by Equations (15) and (16). Further clustering of this ion with H_2O is possible as described by Equation (18). The forward rate for this reaction has not been determined. However, from the value of the equilibrium constant for this reaction and the range of water vapor densities given, an equilibrium ratio of $O_2^-(H_2O)_3/O_2^- (H_2O)_2 > 18$ is to be expected. Thus, if the forward rate for $O_2^- (H_2O)_3$ formation is comparable to that for $O_2^-(H_2O)_2$ formation the ion species observed in the present work is expected to be $O_2^- (H_2O)_3$. Measurements of mass identified ions formed in mixtures of O_2 and H_2O confirm this conclusion (Ref. 12). It is further noted that for humid air containing naturally occurring abundancies of CO_2 ($\sim 0.03\%$) and fractional concentrations of H_2O greater than 0.2% the final ion identity is expected to remain unchanged.

At high values of E/N, the primary negative ions are expected (Ref. 12) to be O^- and H^- formed by the dissociative attachment reactions

$$e + O_2 \rightarrow O^- + O \qquad (19)$$

$$e + H_2O \rightarrow H^- + OH \qquad (20)$$

Further reactions involving the O^- ions, H^- ions, and their progeny are
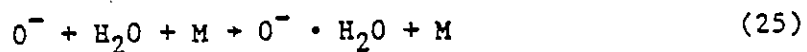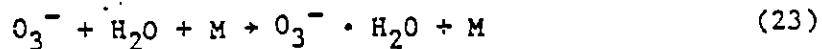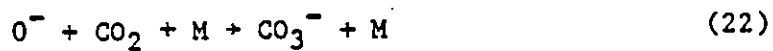
$$O^- + O_2 + M \rightarrow O_3^- + M \tag{21}$$

$$O^- + CO_2 + M \rightarrow CO_3^- + M \tag{22}$$

$$O_3^- + H_2O + M \rightarrow O_3^- \cdot H_2O + M \tag{23}$$

$$O_3^- + CO_2 \rightarrow CO_3^- + O_2 \tag{24}$$

$$O^- + H_2O + M \rightarrow O^- \cdot H_2O + M \tag{25}$$

$$H^- + O_2 \rightarrow e + HO_2 \tag{26}$$

$$H^- + H_2O \rightarrow OH^- + H_2 \tag{27}$$

$$OH^- + CO_2 + M \rightarrow OH^- \cdot CO_2 + M \tag{28}$$

$$OH^- + H_2O + M \rightarrow OH^- \cdot H_2O + M \tag{29}$$

Studies of these reactions have been made with O_2 as the third body (i.e., $M = O_2$). From these studies the thermal rate coefficients have been determined to be $1.1 \times 10^{-42} m^6/s$, $3.1 \times 10^{-40} m^6/s$, $2.7 \times 10^{-40} m^6/s$, $5.5 \times 10^{-16} m^3/s$, $1.3 \times 10^{-40} m^6/s$, $1.2 \times 10^{-15} m^3/s$, $3.7 \times 10^{-15} m^3/s$, $7.6 \times 10^{-40} m^6/s$, and $2.5 \times 10^{-40} m^6/s$, respectively (Refs. 13, 14, 17-19). In addition to the above product ions, more complex clusters of O^-, O_3^-, and OH^- with H_2O may be formed (Refs. 12, 14).

In the present work the value of the negative-ion mobility is found to be a function of E/N for values of $E/N > 6 \times 10^{-20}$ V·m². This indicates that either the negative ions are not in thermal equilibrium with the gas and/or that the identity of the ion species is a function of E/N. It is also noted that, based on the lower values of the mobility in humid air compared with those in dry air, the presence of

water vapor influences the ion identity in this range of E/N. In view of the liklihood that the negative ions are not in thermal equilibrium with the gas it is difficult to predict with certainty the identity of the ion species observed in the present work based on arguments involving thermal reaction rates. Nevertheless, if these rates are taken together with the densities of N_2 ($> 6 \times 10^{22} m^{-3}$), O_2 ($> 1.6 \times 10^{22} m^{-3}$), CO_2 ($< 6 \times 10^{18} m^{-3}$), and H_2O ($> 1.6 \times 10^{21} m^{-3}$) pertaining to the air mixtures used in this range of E/N, the dominant reaction path of ions derived from O^- is expected to lead to the formation of $O^- \cdot H_2O$ and higher order clusters with H_2O via reactions of the type described by Equation (25). On the other hand, for the ratio of $H_2O/O_2 \sim 0.1$ pertaining to the present mixtures, the H^- ions are most likely to suffer detachment reactions according to Equation (26). Thus, even though the attachment rate coefficient for H^- formation is approximately a factor of 2 larger than that for O^- formation at comparable electron mean energies, the contribution of H^- derived ions to the total negative-ion spectrum is expected to be small in the present mixtures. We conclude that the negative-ion species observed in the present measurements for values of E/N $> 6 \times 10^{-20}$ V·m^2 are clusters of O^- with H_2O. Cluster formation in humid air has a significant effect on the measurement of attachment rates and is discussed further in paragraph 5.

3. POSITIVE ION MOBILITIES

In the case of the positive ions, the waveforms do not exhibit a simple exponential time dependence, indicating the presence of more than one positive ion specie or the occurrence of ion conversion reactions. Thus, the values of the positive-ion mobility summarized in Figure 10 and Table 4 refer to the slowest ion, the only specie clearly resolved in the present measurements.

The positive ions formed at electron energies near the threshold for ion production by electron impact are expected to be O_2^+, N_2^+, and H_2O^+ as a result of the reactions

TABLE 4. VALUES OF THE POSITIVE-ION MOBILITY IN HUMID AIR (2.00% H_2O) COMPARED WITH PREVIOUS MEASUREMENTS (REF. 1) IN DRY AIR

E/N		$f(H_2O) = 0$		$f(H_2O) = 0.0200$	
		μ_+N	μ_+N/N_0	μ_+N	μ_+N/N_0
10^{-21} V·m^2	10^4V/m	10^{21}/V·m·s	10^{-4}m^2/V·s	10^{21}/V·m·s	10^{-4}m^2/V·s
80.0	215.0			6.07	2.26
90.0	241.9			6.24	2.32
112.5	302.4	6.83	2.54	6.40	2.38
125.0	336.0	6.88	2.56	6.50	2.42
137.5	369.6	6.91	2.57	6.59	2.45
150.0	403	6.95	2.59	6.67	2.48
175.0	470	6.85	2.55	6.64	2.47
200.0	538	6.73	2.50	6.45	2.40
225.0	605	6.54	2.43	6.26	2.33
250.0	672	6.33	2.35	6.05	2.25
275.0	739	6.11	2.27	5.94	2.21
300.0	806	5.94	2.21	5.78	2.15

$N_o = 2.688 \times 10^{25}$m^{-3}

Estimated uncertainties in the measured quantities are:

E/N: $\pm$ 0.2%; f $= \pm$ 2%

μ_+N, μ_+N/N_o (f = 0): $\pm$ 1%

μ_+N, μ_+N/N_o (f = 0.0200): $\pm$ 1%

$$e + O_2 \rightarrow O_2^+ + 2e \qquad\qquad (30)$$

$$e + N_2 \rightarrow N_2^+ + 2e \qquad\qquad (31)$$

$$e + H_2O \rightarrow H_2O^+ + 2e \qquad\qquad (32)$$

The more probable ion-molecule reactions, and their thermal rate coefficients (Refs. 16, 20-26), that can occur involving these ions are

$$O_2^+ + N_2 + N_2 \rightarrow O_2^+ \cdot N_2 + N_2 \qquad\qquad (8 \times 10^{-43} \ m^6/s) \qquad (33)$$

$$O_2^+ + O_2 + O_2 \rightarrow O_4^+ + O_2 \qquad\qquad (2.5 \times 10^{-42} \ m^6/s) \qquad (34)$$

$$O_2^+ \cdot N_2 + O_2 \rightarrow O_4^+ + O_2 \qquad\qquad (5 \times 10^{-17} \ m^3/s) \qquad (35)$$

$$O_2^+ + H_2O + N_2 \rightarrow O_2^+ \cdot H_2O + N_2 \qquad\qquad (2.5 \times 10^{-40} \ m^6/s) \qquad (36)$$

$$O_2^+ + H_2O + O_2 \rightarrow O_2^+ \cdot H_2O + O_2 \qquad\qquad (2.3 \times 10^{-40} \ m^6/s) \qquad (37)$$

$$O_2^+ \cdot N_2 + H_2O \rightarrow O_2^+ \cdot H_2O + N_2 \qquad\qquad (4 \times 10^{-15} \ m^3/s) \qquad (38)$$

$$O_4^+ + H_2O \rightarrow O_2^+ \cdot H_2O + O_2 \qquad\qquad (1.5 \times 10^{-15} \ m^3/s) \qquad (39)$$

$$O_2^+ \cdot H_2O + H_2O \rightarrow H_3O^+ \cdot OH + O_2 \qquad\qquad (1.2 \times 10^{-15} \ m^3/s) \qquad (40)$$

$$N_2^+ + N_2 + N_2 \rightarrow N_4^+ + N_2 \qquad\qquad (5 \times 10^{-41}) \ m^6/s) \qquad (41)$$

$$N_2^+ + O_2 \rightarrow O_2^+ + N_2 \qquad\qquad (5.1 \times 10^{-17} \ m^3/s) \qquad (42)$$

$$N_2^+ + CO_2 \rightarrow CO_2^+ + N_2 \qquad\qquad (7.7 \times 10^{-16} \ m^3/s) \qquad (43)$$

$$CO_2^+ + O_2 \rightarrow O_2^+ + CO_2 \qquad\qquad (5.6 \times 10^{-17} \ m^3/s) \qquad (44)$$

$$N_4^+ + O_2 \rightarrow O_2^+ + N_2 + N_2 \qquad (2.5 \times 10^{-16} \text{ m}^3/\text{s}) \quad (45)$$

$$N_4^+ + H_2O \rightarrow H_2O^+ + N_2 + N_2 \qquad (3 \times 10^{-15} \text{ m}^3/\text{s}) \quad (46)$$

$$N_2^+ + H_2O \rightarrow H_2O^+ + N_2 \qquad (2.2 \times 10^{-15} \text{ m}^3/\text{s}) \quad (47)$$

$$H_2O^+ + O_2 \rightarrow O_2^+ + H_2O \qquad (2 \times 10^{-16} \text{ m}^3/\text{s}) \quad (48)$$

$$H_2O^+ + H_2O \rightarrow H_3O^+ + OH \qquad (1.8 \times 10^{-15} \text{ m}^3/\text{s}) \quad (49)$$

$$H_3O^+ + H_2O + N_2 \rightarrow H_3O^+ \cdot H_2O + N_2 \qquad (3.4 \times 10^{-39} \text{ m}^6/\text{s}) \quad (50)$$

$$H_3O^+ + H_2O + O_2 \rightarrow H_3O^+ \cdot H_2O + O_2 \qquad (3.7 \times 10^{-39} \text{ m}^6/\text{s}) \quad (51)$$

$$H_3O^+ \cdot OH + H_2O \rightarrow H_3O^+ \cdot H_2O + OH \qquad (1.4 \times 10^{-15} \text{ m}^3/\text{s}) \quad (52)$$

In addition to these product ions, more complex clusters of H_2O^+ with H_2O may be formed. It may be seen that these reaction schemes for the primary ions O_2^+, N_2^+, and H_2O^+ all lead to the formation of clusters of H_3O^+ ions with water. At values of electron energy a few electron volts above the thresholds for N_2^+, O_2^+, and H_2O^+ formation, N^+, O^+, and OH^+ ions are formed by dissociative ionization. Further reactions of these ions lead to the additional ion species NO^+ and CO^+ and clusters of these ions with H_2O.

The values of positive-ion mobility determined in humid air are found to be a function of E/N and also are different from the values determined in dry air. Thus, the ion identity is influenced by the presence of water vapor and the observed ions are probably not in thermal equilibrium with the gas over the range of E/N covered by the present measurements. Thus, while the application of thermal reaction rates to the interpretation of ion identity is questionable, the common product ion of the different reaction schemes makes it probable that the ions observed are H_3O^+ clusters with H_2O.

4. THREE-BODY ATTACHMENT COEFFICIENT

Measurements of the three-body attachment coefficient have been determined over the range $0.6 < E/N < 30 \times 10^{-21}$ V·m^2 and a summary of these values is given in Figure 11. The present measurements have an estimated uncertainty of $\pm$ 5% and the values reported represent the mean of three or more measurements at each value of E/N, the spread being less than the specified uncertainty. Measurements carried out at different gas densities for a given value of E/N have established the quadratic dependence of the attachment coefficient on gas density.

In Figure 11 the present measurements are compared with the data of van Lint (Ref. 7) for humid air having the same fractional concentration of water vapor (2%) and with the previous measurements in dry air (Ref. 1). The values of the effective attachment rate coefficient summarized in Figure 12 and in Table 5, are obtained by combining the measurements of η/N^2 with the measurements of w_e. These values have an estimated uncertainty of $\pm$ 7%.

For values of $E/N < 2 \times 10^{-21}$ V·m^2 the attachment rate coefficient is found to be constant, having a mean value of $(1.53 \pm 0.11) \times 10^{-43}$ m^6/s. Such a behavior is consistent with that observed in the measurements of electron mobility and further corroborates the interpretation that in this region of E/N, the electrons are in thermal equilibrium with the gas. The solid arrow on the left ordinate of Figure 12 indicates the value of the thermal attachment frequency in humid air (f = 0.02) deduced using recent measurements in oxygen and oxygen-nitrogen mixtures (Ref. 27) and in oxygen-water vapor mixtures (Ref. 2), i.e., from

$$k_a = v_a/N^2 = \eta w_e/N^2 = 0.0424 \ k_1 + 0.159 \ k_2 + 0.00412 \ k_3 \qquad (53)$$

In Equation (53), k_1, k_2 and k_3 are the thermal attachment rate coefficients for oxygen, nitrogen and water vapor, respectively, as the third body, and a density ratio of nitrogen to oxygen to water vapor of
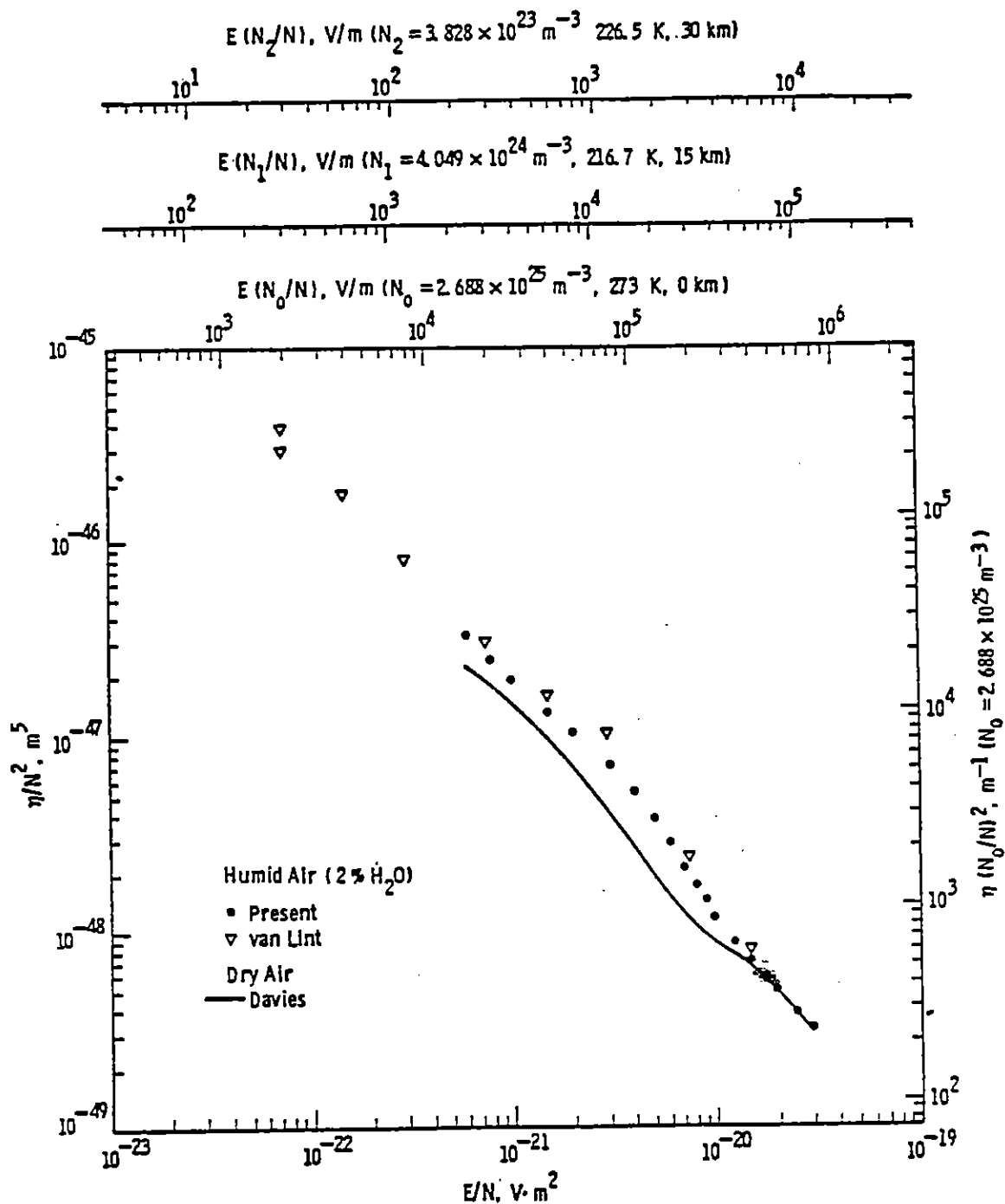
Figure 11. Comparison of the present measurements of the three-body
attachment coefficient as a function of E/N with previous
data in humid air containing the same water vapor concentration.
The solid curve corresponds to previous measurements in
dry air.
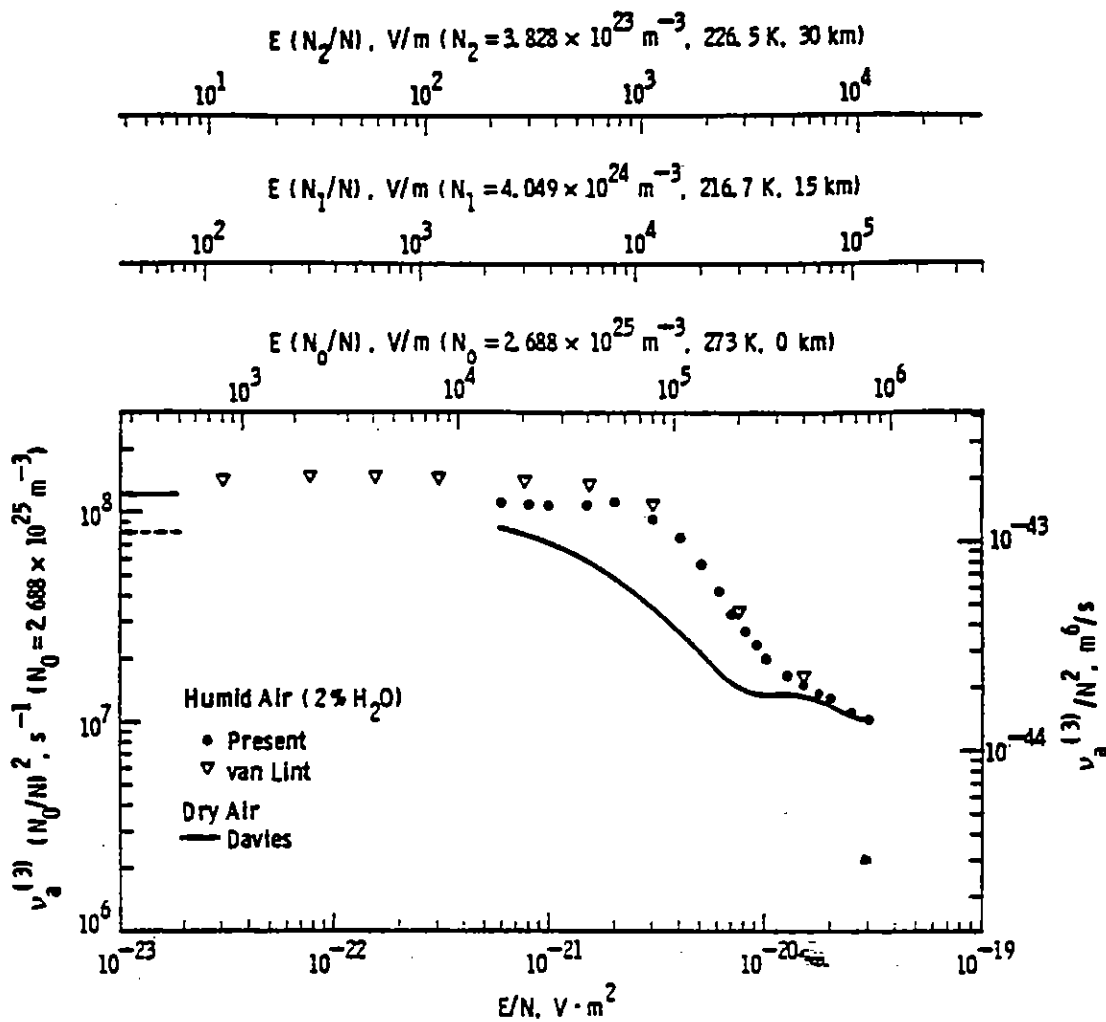
Figure 12. Comparison of the present measurements of the three-body attachment rate coefficient as a function of E/N with previous data in humid air containing the same water vapor concentration. The solid curve corresponds to previous measurements in dry air. The dashed and solid arrows on the ordinate correspond to the thermal value of the rate coefficient in dry air and humid air (2% H_2O), respectively, deduced from previous measurements in oxygen and mixtures of oxygen with nitrogen and water vapor.

41

TABLE 5. VALUES OF THE THREE-BODY ATTACHMENT RATE IN HUMID AIR (2.00% H_2O) COMPARED WITH PREVIOUS MEASUREMENTS (REF. 1) IN DRY AIR

E/N	EN_o/N	$f(H_2O) = 0$		$f(H_2O) = 0.0200$	
		$\nu_a^{(3)} N_o^2/N^2$	$\nu_a^{(3)}/N^2$	$\nu_a^{(3)} N_o^2/N^2$	$\nu_a^{(3)}/N^2$
10^{-21} V·m^2	10^4 V/m	10^7/s	10^{-44} m^6/s	10^7/s	10^{-44} m^6/s
0.600	1.613	8.4	11.7	11.1	15.3
0.800	2.150	7.8	10.7	11.0	15.3
1.000	2.688	7.2	9.9	10.9	15.1
1.500	4.03	5.8	8.1	11.0	15.2
2.000	5.38	4.8	6.6	11.3	15.7
3.000	8.06	3.5	4.8	9.2	12.8
4.00	10.75	2.60	3.6	7.6	10.5
5.00	13.44	2.15	2.97	5.7	7.9
6.00	16.13	1.78	2.46	4.3	5.9
7.00	18.82	1.51	2.09	3.3	4.5
8.00	21.50	1.46	2.02	2.70	3.7
9.00	24.19	1.36	1.88	2.32	3.2
10.00	26.88	1.35	1.87	2.04	2.83
12.50	33.60	1.35	1.87	1.68	2.33
15.00	40.3	1.31	1.81	1.48	2.05
17.50	47.0	1.24	1.71	1.34	1.86
20.00	53.8	1.18	1.63	1.27	1.75
25.00	67.2	1.05	1.45	1.09	1.51
30.00	80.6	1.01	1.40	1.00	1.39

$N_o = 2.688 \times 10^{25}$ m^{-3}

Estimated uncertainties in the measured quantities are:

E/N: $\pm$ 0.2%; f: $\pm$ 2%

$\nu_a^{(3)}/N^2$, $\nu_a^{(3)} N_o^2/N^2$ (f = 0): $\pm$ 6%

$\nu_a^{(3)}/N^2$, $\nu_a^{(3)} N_o^2/N^2$ (f = 0.0200): $\pm$ 7%

77.4/20.6/2 has been assumed. Thus, using the values of $k_1 = 2.2 \times 10^{-42}$ m^6/s, $k_2 = 1.1 \times 10^{-43}$ m^6/s (Ref. 27), and $k_3 = 1.4 \times 10^{-41}$ m^6/s (Ref. 2), gives a value of $k_a = 1.68 \times 10^{-43}$ m^6/s. Also shown for comparison in Figure 12 by the dashed arrow on the left ordinate is the thermal attachment frequency in dry air, 1.15×10^{-43} m^6/s, deduced from

$$k_a = 0.0441 \ k_1 + 0.166 \ k_2 \qquad (54)$$

using the same values of k_1 and k_2 and assuming a density ratio of nitrogen to oxygen of 79/21.

The present value for the thermal attachment frequency in humid air is 30% lower than that determined by van Lint (Ref. 7) but is in agreement, to within the combined experimental uncertainty, with the value 1.68×10^{-43} m^6/s deduced from Equation (53). The present values of attachment frequency at higher values of.E/N are also lower than those determined by van Lint. From the measurements of Hegerberg and Crompton (Ref. 27), it is unlikely that the attachment cooling effect may be invoked to explain the difference between the present thermal attachment frequency and that measured by van Lint. The fractional concentration of water vapor in the mixture is large enough to ensure that the energy exchange collision frequency (which is dominated at low E/N by the water vapor) is sufficiently larger than the attachment frequency to prevent distortion of the electron energy distribution by inadequate thermalization. No evidence for a peak in the attachment-frequency is found in the present work in humid air in contrast to the observations in dry air (Refs. 28, 29).

Previous values reported for the thermal attachment rate coefficients k_1 and k_2 are subject to smaller uncertainties than that for k_3. Thus, the present value of $k_a = 1.53 \times 10^{-43}$ m^6/s for the effective thermal attachment rate coefficient in the humid air mixture may be used with the previous measurements of k_1 and k_2 (Ref. 27) to determine k_3 from Equation (53). A value of $k_3 = (1.0 \pm 0.2) \times 10^{-41}$ m^6/s is found which is 30% lower than that reported previously (Ref. 2).

Further measurements in humid air having higher water vapor concentrations would be desirable to further reduce the uncertainty in the value of k_3.
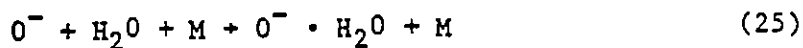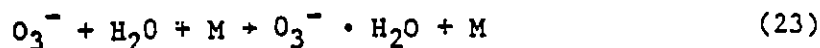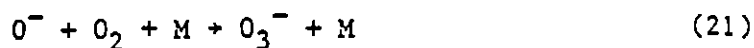
5. TWO-BODY ATTACHMENT AND IONIZATION COEFFICIENTS

In paragraph 2 it has been noted that the primary negative ions formed in the range of $E/N > 6 \times 10^{-20}$ $V \cdot m^2$ are O^- and H^- produced in the two-body dissociative attachment reactions described by Equations (19) and (20). Moreover, it appears that the collisional detachment channel described by Equation (26) is the most probable reaction path of the H^- ions. On the other hand, in the case of the O^- ions, collisional three-body conversion reaction rates are sufficiently large that, over an experimentally accessible density range, reaction channels leading to the formation of the more stable negative ions are favored over the detachment reaction channel.

For dry air it has been found that the two-body attachment rate increases initially with increasing E/N over the range $60 < E/N < 100 \times 10^{-21}$ $V \cdot m^2$ but decreases rapidly with further increasing E/N above 100×10^{-21} $V \cdot m^2$ (Ref. 1). In addition, it has been noted that this behavior is contrary to the monotonically increasing attachment rate with increasing E/N predicted over this range of E/N from a Boltzmann analysis using presently known electron collision cross sections for N_2 and O_2.[*] The increasing divergence between the measured and predicted attachment rates for $E/N > 100 \times 10^{-21}$ $V \cdot m^2$ has been attributed to the increasing importance of collisional detachment over this range of E/N (Ref. 1).

The presence of H_2O in the humid air mixtures used in the present work provides an additional important ion conversion channel through the reaction described by Equation (25). Thus, in the case of humid air, the predominant reaction channels for the O^- ions are

---

[*]L. E. Kline, private communication.

44

$$O^- + O_2 + M \rightarrow O_3^- + M \qquad\qquad (21)$$

$$O_3^- + H_2O + M \rightarrow O_3^- \cdot H_2O + M \qquad\qquad (23)$$

$$O^- + H_2O + M \rightarrow O^- \cdot H_2O + M \qquad\qquad (25)$$

$$O^- + M \rightarrow O + M + e \qquad\qquad (55)$$

Further three-body reactions involving $O^- \cdot H_2O$ and $O_3^- \cdot H_2O$ with H_2O lead to higher order cluster ions. The formation of cluster ions decreases the probability of collisional detachment as a result of (a) the decreased mean energy of the more massive cluster ions and (b) the additional degrees of freedom for energy conservation in ion-molecule collisions provided by successive detachment of H_2O molecules. Nevertheless, as in the case of dry air (Ref. 1), the measured attachment coefficient is regarded as an effective coefficient which is a function of the true attachment coefficient, the charge transfer coefficients and the detachment coefficient. Increasing the gas density favors the three-body ion conversion reactions relative to the two-body detachment reaction. Thus, to minimize detachment effects in the present study, measurements have been made at the maximum values of gas density consistent with electrical breakdown constraints.

The values of the net ionization coefficient determined as a function of E/N from either the negative-ion or positive-ion waveforms are given in Table 6 together with their estimated uncertainties and plotted as absolute values in Figure 13 where they are compared with previous measurements in dry air (Ref. 1). For values of E/N < 70 x 10^{-21} V·m^2, no positive ions are detected and the data in this region correspond to pure attachment coefficients.

The present measurements of α/η, which are given in Table 6, have been determined directly from the ratio of the positive charge to negative charge collected as described previously (Ref. 1), i.e., neglecting detachment effects. The estimated uncertainty in this ratio

TABLE 6. SUMMARY OF THE SWARM PARAMETERS DETERMINED IN HUMID AIR (2.00% H₂O)

E/N 10^{-21}V·m²	v_e m/s	μ_e m²/V·s	μ_- 10^{-4}m²/V·s	μ_+ 10^{-4}m²/V·s	$\eta^{(3)}/N^2$ 10^{-48}m⁵	$k_a^{(3)}$ 10^{-42}m⁶/s	$(\alpha-\eta)/N$ 10^{-22}m²	α/η	$\eta^{(2)}/N$ 10^{-22}m²	$k_a^{(c)}$ 10^{-18}m³/s	α/N 10^{-22}m²	k_I 10^{-18}m³/s
0.600	4.46×10^3	0.277	1.85		34.4	15.3						
0.700	5.23×10^3	0.278										
0.800	5.99×10^3	0.279	1.85		25.5	15.3						
0.900	6.80×10^3	0.281										
1.000	7.58×10^3	0.282	1.86		20.0	15.1						
1.250	9.26×10^3	0.276										
1.500	1.11×10^4	0.275	1.86		13.7	15.2						
1.750	1.31×10^4	0.279										
2.000	1.48×10^4	0.275	1.85		10.6	15.7						
2.500	1.75×10^4	0.260										
3.000	1.79×10^4	0.222	1.86		7.1	12.8						
3.500	1.92×10^4	0.204										
4.00	2.02×10^4	0.188	1.85		5.2	10.5						
4.50	2.03×10^4	0.168										
5.00	2.06×10^5	0.153	1.85		3.8	7.9						
6.00	2.05×10^6	0.127	1.85		2.90	5.9						
7.00	2.11×10^4	0.112	1.85		2.15	4.5						
8.00	2.16×10^6	0.100	1.85		1.73	3.7						
9.00	2.24×10^4	0.0926	1.86		1.43	3.2						
10.00	2.36×10^4	0.0878	1.86		1.20	2.83						
12.50	2.62×10^4	0.0780	1.86		0.89	2.33						
15.00	2.94×10^4	0.0729	1.86		0.70	2.05						
17.50	3.22×10^4	0.0685	1.87		0.58	1.86						
20.00	3.56×10^4	0.0662	1.86		0.49	1.75						
25.00	4.04×10^4	0.0601	1.86		0.37	1.51						
30.00	4.43×10^4	0.0549	1.87		0.31	1.39						
35.00	5.00×10^4	0.0531	1.85									
40.00	5.57×10^4	0.0518	1.86									
50.00	6.66×10^4	0.0496										
60.00			2.47				$-0.076 \pm 7\%$		$0.076 \pm 7\%$	$0.57 \pm 8\%$		
70.00	8.48×10^4	0.0451	2.57				$-0.142 \pm 5\%$		$0.142 \pm 5\%$	$1.20 \pm 6\%$		
80.00			2.64	2.26			$-0.142 \pm 5\%$	0.31	$0.206 \pm 6\%$	$2.0 \pm 7\%$	$0.064 \pm 8\%$	$0.61 \pm 9\%$
90.00			2.68	2.32			$-0.122 \pm 7\%$	0.52	$0.254 \pm 10\%$	$2.8 \pm 11\%$	$0.132 \pm 11\%$	$1.44 \pm 12\%$
100.0	1.19×10^5	0.0443										
112.5			2.75	2.38								
125.0			2.78	2.42			$0.40 \pm 5\%$	2.10	$0.36 \pm 9\%$	$5.3 \pm 11\%$	$0.76 \pm 7\%$	$11.1 \pm 9\%$
137.5			2.79	2.45			$0.74 \pm 3\%$	2.97	$0.35 \pm 6\%$	$5.9 \pm 8\%$	$1.12 \pm 4\%$	$17.5 \pm 6\%$
150.0	1.69×10^5	0.0419	2.80	2.48			$1.20 \pm 3\%$	4.1	$0.39 \pm 6\%$	$6.4 \pm 8\%$	$1.59 \pm 4\%$	$26.7 \pm 6\%$
175.0			2.79	2.47			$2.71 \pm 3\%$	7.5	$0.42 \pm 5\%$	$8.2 \pm 7\%$	$3.13 \pm 3\%$	$61 \pm 5\%$
200.0	2.19×10^5	0.0407	2.75	2.40			$4.8 \pm 3\%$	12.1	$0.43 \pm 5\%$	$9.4 \pm 7\%$	$5.2 \pm 3\%$	$114 \pm 5\%$
225.0			2.65	2.33			$8.1 \pm 3\%$				$8.1 \pm 3\%$	$192 \pm 5\%$
250.0	2.54×10^5	0.0378		2.25			$11.1 \pm 3\%$				$11.1 \pm 3\%$	$282 \pm 5\%$
275.0				2.21			$13.5 \pm 3\%$				$13.5 \pm 3\%$	$369 \pm 5\%$
300.0	2.94×10^5	0.0365		2.15			$17.6 \pm 3\%$				$17.6 \pm 3\%$	$517 \pm 5\%$

‡ Net ionization coefficient

Thermal μ_e: (0.278 ± 0.006) m²/V·s   Thermal $k_a^{(3)}$: $(1.53 \pm 0.11) \times 10^{-43}$ m⁶/s

Estimated uncertainties in the measured quantities are:

E/N: ± 0.2%

f: ± 2%

v_e, μ_e: ± 1% for $10^{-20} \leq$ E/N $\leq 10^{-19}$ V·m²
   ± 2% for E/N < 10^{-20} V·m² and E/N > 10^{-19} V·m²

μ_-, v_+: ± 1%

$\eta^{(3)}/N^2$: ± 6%

$k_a^{(3)}$: ± 7%

α/η: ± 2%

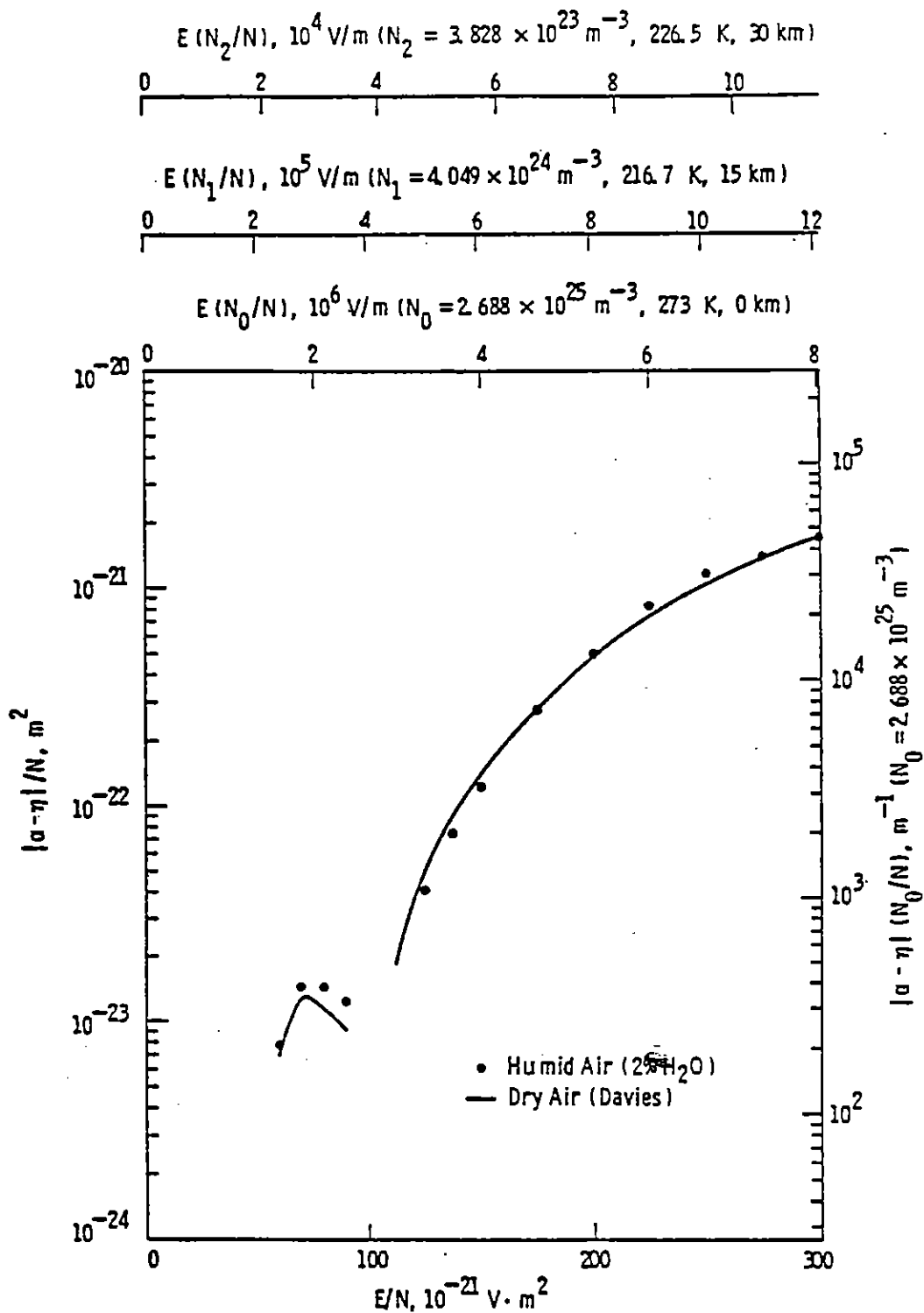$(\alpha-\eta)/N$, $\eta^{(2)}/N$, $k_a^{(2)}$, α/N, k_I: As noted in table

46

Figure 13. Comparison of the present values (solid points) of the net ionization coefficient as a function of E/N with previous measurements (solid curve) in dry air.

is ± 2%. Combining these measurements with the values of the net ionization coefficient gives the coefficients for two-body attachment and ionization given in Table 6 and Figure 14 where they are compared with previous measurements in dry air (Ref. 1). The data for the individual coefficients are confined to values of $E/N < 200 \times 10^{-21}$ V·m^2 for which the ratio α/n may be determined accurately. For higher values of E/N, the data correspond to net ionization coefficients. Combining the values of α/N and $n^{(2)}/N$ with the values of w_e given in Table 2 gives the rate coefficients for two-body attachment and ionization shown in Figure 15 and in Tables 7 and 8.

The measurements of two-body attachment in humid air shown in Figures 14 and 15 are significantly different from those in dry air determined previously (Ref. 1), particularly for values of $E/N >$ 100×10^{-21} V·m^2. However, the data for humid air are in good agreement with the values for 0^- production predicted from solutions to the Boltzmann transport equation.[*] This gives greater credance to the previous interpretation that collisional detachment in dry air is responsible for the comparatively lower values of attachment measured in dry air. Although detachment effects are clearly much smaller in the present measurements in humid air, the measurements are still regarded as effective values. For this reason, the values of gas density at which the measurements were made have been included in Tables 7 and 8.

Further measurements in humid air mixtures having different water vapor concentrations would provide further information on the branching ratio of ion conversion to detachment. It is evident from the previous measurements in dry air and the present ones in humid air that this ratio is sensitive to variations in water vapor concentration over the range from 0 to 2%. This suggests that a series of measurements of the effective attachment rate as a function of water vapor concentration at constant E/N could provide a convenient method of determining the branching ratio of ion conversion to detachment as a function of E/N.

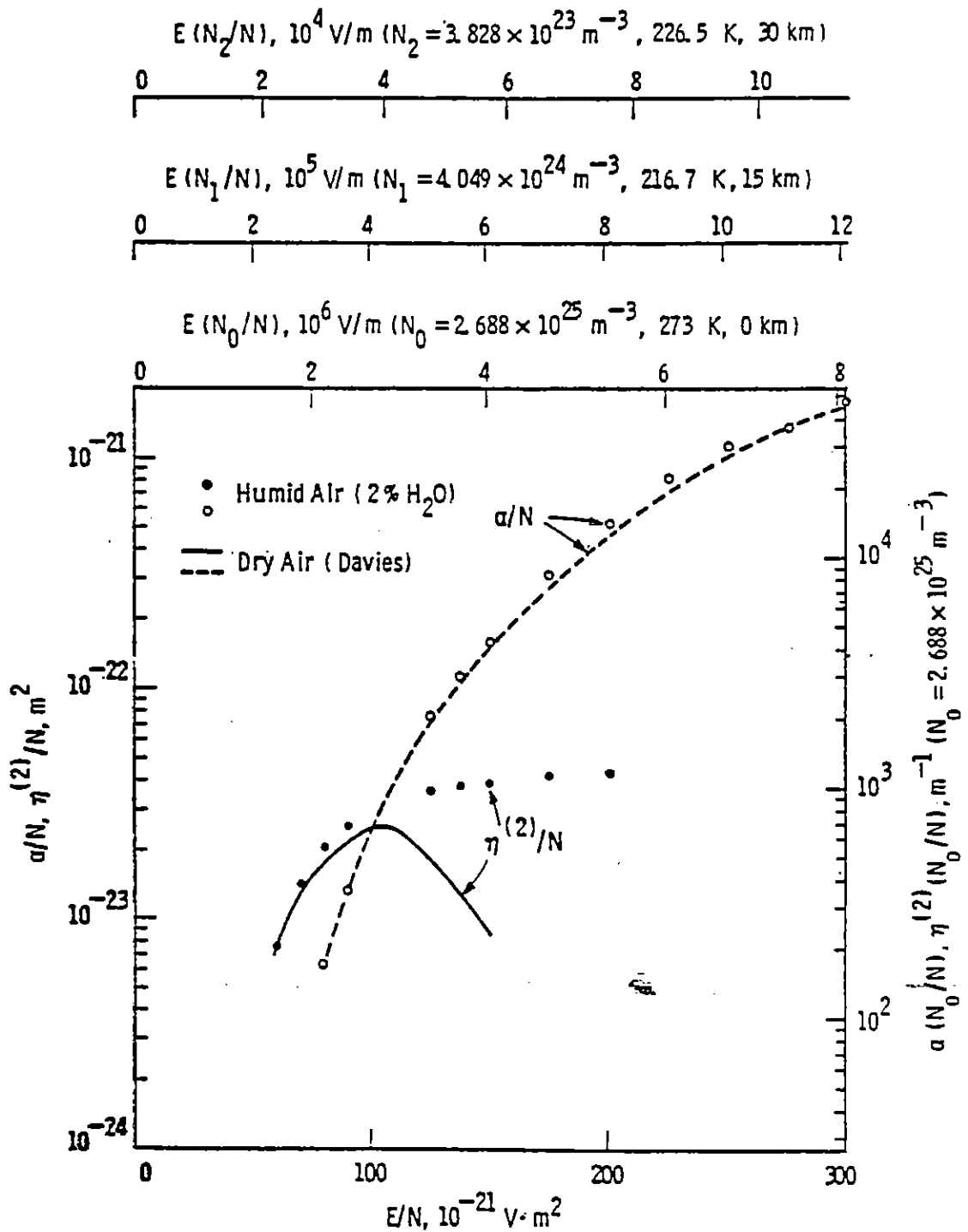---

[*]L. E. Kline, private communication.

Figure 14. Comparison of the present measurements of the two-body attachment (solid points) and ionization coefficient (open points) as a function of E/N with previous measurements (solid and dashed curves, respectively) in dry air.

$E(N_2/N)$, 10^4 V/m ($N_2 = 3.828 \times 10^{23}$ m^{-3}, 226.5 K, 30 km)

$E(N_1/N)$, 10^5 V/m ($N_1 = 4.049 \times 10^{24}$ m^{-3}, 216.7 K, 15 km)

$E(N_0/N)$, 10^6 V/m ($N_0 = 2.688 \times 10^{25}$ m^{-3}, 273 K, 0 km)

• Humid Air (2% H$_2$O)
○
─── Dry Air (Davies)

ν_i

$\nu(N_0/N)$, s^{-1} ($N_0 = 2.688 \times 10^{25}$ m^{-3})

ν/N, m^3/s

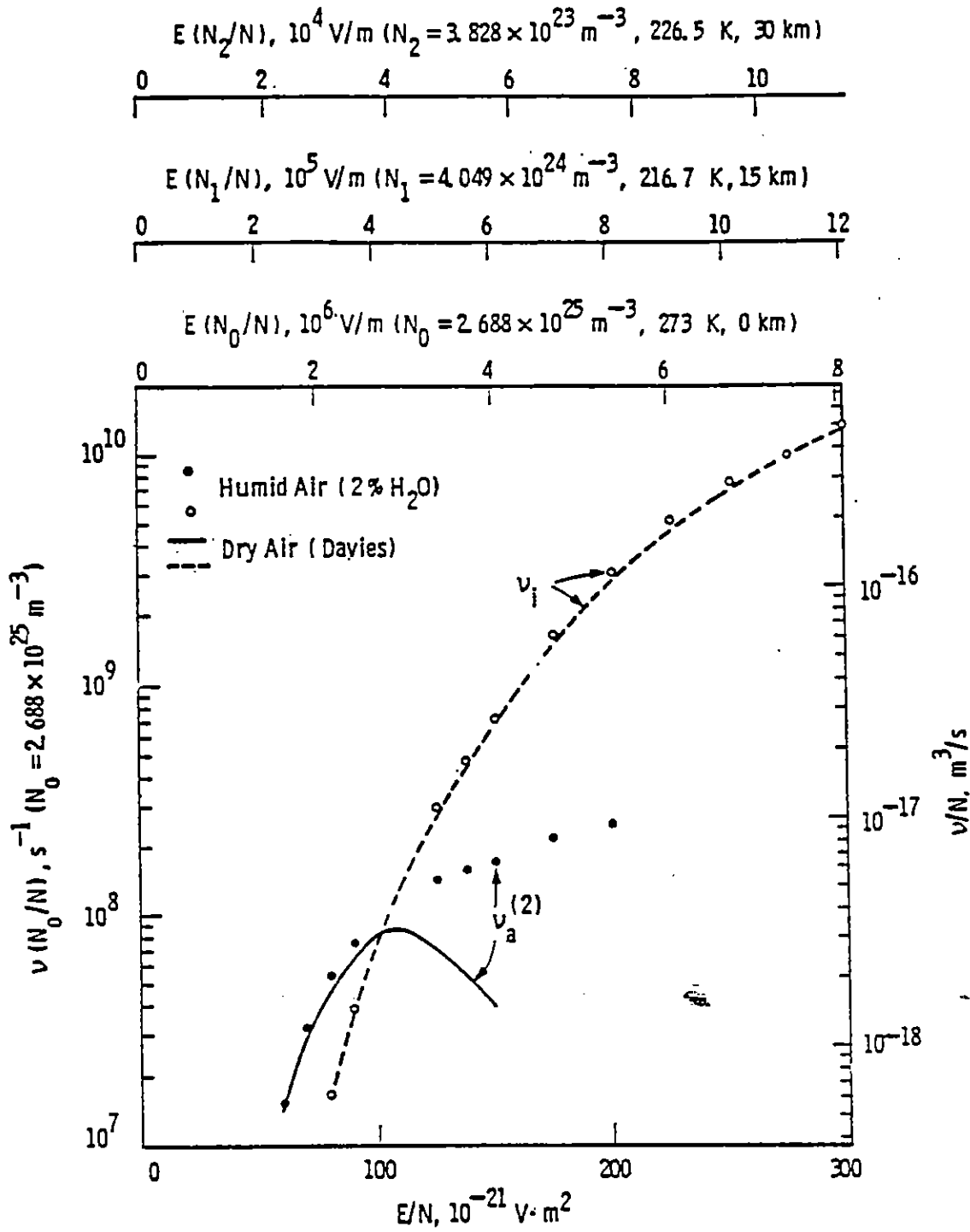$\nu_a^{(2)}$

E/N, 10^{-21} V·m^2

Figure 15. Comparison of the present measurements of the two-body
attachment rate coefficient (solid points) and ionization
rate coefficient (open points) as a function of E/N with
previous measurements (solid and dashed curves, respectively)
in dry air.

50

TABLE 7. VALUES OF THE TWO-BODY ATTACHMENT RATE IN HUMID AIR (2.00% H_2O)

N $10^{22}m^{-3}$	E/N $10^{-21}V \cdot m^2$	EN_0/N $10^4 V/m$	$\nu_a^{(2)}N_0/N$ $10^7/s$	$\nu_a^{(2)}/N$ $10^{-18}m^3/s$
138.5	60.0	161.3	1.53 $\pm$ 8%	0.57 $\pm$ 8%
138.5	70.0	188.2	3.2 $\pm$ 6%	1.20 $\pm$ 6%
138.5	80.0	215.0	5.4 $\pm$ 7%	2.0 $\pm$ 7%
76.2	90.0	241.9	7.5 $\pm$ 11%	2.8 $\pm$ 11%
32.6	125.0	336.0	14.2 $\pm$ 11%	5.3 $\pm$ 11%
32.6	137.5	369.6	15.9 $\pm$ 8%	5.9 $\pm$ 8%
32.6	150.0	403	17.2 $\pm$ 8%	6.4 $\pm$ 8%
7.81	175.0	470	22.0 $\pm$ 7%	8.2 $\pm$ 7%
7.81	200.0	538	25.3 $\pm$ 7%	9.4 $\pm$ 7%

$N_o = 2.688 \times 10^{25}m^{-3}$

Estimated uncertainties in the measured quantities are:

E/N: $\pm$ 0.2%; f: $\pm$ 2%

$\nu_a^{(2)}/N$, $\nu_a^{(2)}N_o/N$: As noted in table

TABLE 8.   VALUES OF THE IONIZATION RATE IN HUMID AIR (2.00% H_2O)

N $10^{22}m^{-3}$	E/N $10^{-21}v\cdot m^2$	EN_o/N $10^4 v/m$	$\nu_i N_o/N$ $10^7/s$	ν_i/N $10^{-18}m^3/s$
138.5	80.0	215.0	1.64 $\pm$ 9%	0.61 $\pm$ 9%
76.2	90.0	241.9	3.87 $\pm$ 12%	1.44 $\pm$ 12%
32.6	125.0	336.0	29.8 $\pm$ 9%	11.1 $\pm$ 9%
32.6	137.5	369.6	47 $\pm$ 6%	17.5 $\pm$ 6%
32.6	150.0	403	72 $\pm$ 6%	26.7 $\pm$ 6%
7.81	175.0	470	164 $\pm$ 5%	61 $\pm$ 5%
7.81	200.0	538	306 $\pm$ 5%	114 $\pm$ 5%
7.81	225.0	605	516 $\pm$ 5%	‡ 192 $\pm$ 5%
3.53	250.0	672	758 $\pm$ 5%	‡ 282 $\pm$ 5%
3.53	275.0	739	992 $\pm$ 5%	‡ 369 $\pm$ 5%
3.53	300.0	806	1390 $\pm$ 5%	‡ 517 $\pm$ 5%

N_o = 2.688 x $10^{25}m^{-3}$ ‡ Net ionization rate coefficient

Estimated uncertainties in the measured quantities are:

E/N = $\pm$ 0.2%; f = $\pm$ 2%

ν_i/N, $\nu_i N_o/N$:   As noted in table

The analysis of such data is particularly straightforward (and less ambiguous) if the production rate of O^- is independent of water vapor concentration at constant E/N. For this to be true the contribution of the electron collision cross sections in water vapor in determining the electron energy distribution in humid air over the range of E/N > 60 x 10^{-21} V·m^2 must be small. That such is the case is suggested by the fact that the electron drift velocity in this range of E/N is the same for dry air and for humid air with 2% H_2O (cf. Table 2 and Figure 9) and also by the independence of values of $\alpha-\eta^{(2)}$, determined by a different technique (Ref. 30), to water vapor concentration over the range from 0.06% to 1.3%.

6. DISCUSSION

The present data represent a comprehensive set of measurements of the swarm parameters in humid air containing 2% water vapor. This concentration corresponds to saturated air at a temperature of 291 K. The complete data base for this mixture determined in the present study is summarized in Table 6. A plot of the three- and two-body attachment frequencies together with the ionization frequency corresponding to atmospheric density at 0 km and 273 K (2.688 x 10^{25} m^{-3}) is shown in Figure 16 compared with previous measurements in dry air (Ref. 1).

Figures 16 and 17 clearly identify the two regions of E/N over which the swarm parameters in air are particularly sensitive to water vapor concentration, i.e., E/N < 25 x 10^{-21} V·m^2 and E/N > 100 x 10^{-21} V·m^2. It has already been pointed out in paragraph 5 that further measurements in air at high E/N for different water vapor concentrations would enable the branching ratio of ion conversion to detachment to be determined as a function of E/N. At low values of E/N, additional measurements for different water vapor concentrations would enable the thermal mobility of electrons and the thermal rate for three-body attachment in dry air to be determined.
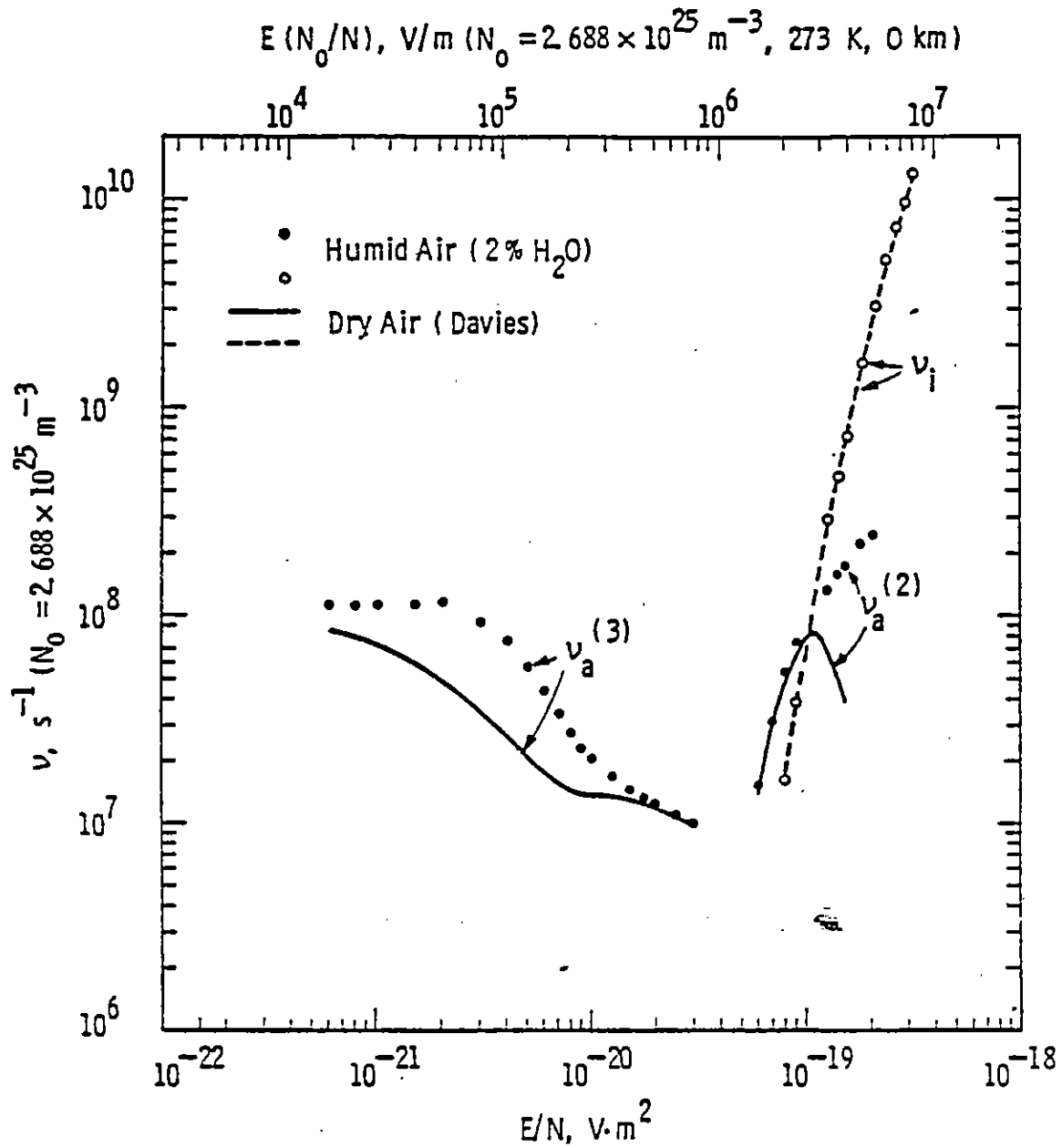
53

Figure 16. Present measurements of the attachment and ionization
frequencies normalized to atmospheric density at 0 km
and 273 K (N_0 = 2.688 x $10^{25} m^{-3}$) as a function of E/N
compared with previous measurements in dry air.

7. ESTIMATES OF MEASUREMENT UNCERTAINTIES

The estimation of uncertainties in the present measurements follows the detailed analysis given previously (Ref. 1). However, in the case of humid air there is an additional uncertainty introduced in the measured coefficients due to the uncertainty in mixture composition, specifically, the water vapor concentration. Clearly, the effect of the uncertainty in water vapor concentration is only significant under conditions where the water vapor has a significant effect on the measured coefficients. Thus, the estimated uncertainties are the same as those for dry air where there is little or no effect on the measured coefficients due to the presence of water vapor. For conditions where the water vapor affects the coefficients, estimation of the additional uncertainty requires a knowledge of the functional dependence of the particular coefficient on water vapor concentration at each value of E/N. In the absence of such information, a linear dependence of each coefficient on water vapor concentration has been assumed defined at each value of E/N by the values determined in dry air and in the humid air (2% H_2O) mixture. The resulting uncertainties in the swarm parameters for humid air are estimated to be

$\mu_e N$, $\mu_e N/N_o$: $\pm$ 1% for $10^{-20} < E/N < 10^{-19}$ V·m^2

   $\pm$ 2% for E/N $< 10^{-20}$ V·m^2 and E/N $> 10^{-19}$ V·m^2

$\mu_- N$, $\mu_- N/N_o$: $\pm$ 1%

$v_a^{(3)}/N^2$, $v_a^3 N_o^2/N^2$: $\pm$ 7%

$(\alpha-\eta)/N, v_a^{(2)}/N$, v_i/N: As noted in Tables 6, 7 and 8

IV. RECOMMENDATIONS

The present measurements in humid air (2% H_2O) together with the previous data in dry air (Ref. 1) provide comprehensive sets of measurements for two values of humidity of interest in air chemistry codes. Additional measurements in humid air with different concentrations of water vapor would be desirable to determine the functional dependence of the swarm parameters on water vapor concentration over the regions of $E/N \leq 25 \times 10^{-21}$ $V \cdot m^2$ and $\geq 100 \times 10^{-21}$ $V \cdot m^2$ where the effects of water vapor are most significant. Such measurements would provide data on

(a) The mobility of thermal electrons in dry air.

(b) The attachment rate of thermal electrons in dry air.

(c) The effectiveness of water vapor as a third body in the three-body attachment process as a function of E/N.

(d) The branching ratio of ion conversion to detachment for O^- ions as a function of E/N.

All of these processes may be investigated using the present drift-tube facility which has the capability for in-situ monitoring of the water vapor concentration. Studies of electron detachment would be particularly desirable in view of the large spread (three orders of magnitude) in the detachment rates that have been reported in the literature (Refs. 30-37).

In addition, further measurements would be desirable on the following processes:

(e) The effect on the measured swarm parameters of high-energy irradiation of the air samples by cascading of the high-energy electrons to energies in equilibrium with the drift field.

(f) The positive-ion mobility at low values of E/N below the onset
     of avalanche ionization.

(g) The recombination rate as a function of E/N.

These processes may be investigated using the present drift-tube
facility by coupling an electron gun to the system and injecting a high-
energy electron beam into the drift region. To provide the flexibility
in the properties of the electron beam necessary for studying processes
(e)-(g) requires the construction of an electron gun. The preliminary
design of a suitable gun has been described previously (Ref. 38).

REFERENCES

1. Davies, D. K.. "Measurements of Swarm Parameters in Dry Air,"
    Theoretical Note 346, May 1983.

2. Pack, J. L. and Phelps, A. V., "Electron Attachment and
    Detachment. II. Mixtures of O_2 and CO_2 and of O_2 and H_2O," J.
    Chem. Phys. 45, 4316-4329 (1966).

3. Watanabe, K. and Zelikoff, M., "Absorption Coefficients of Water
    Vapor in the Vacuum Ultraviolet," J. Opt. Soc. Am. 43, 753-755
    (1953).

4. Watanabe, K., Inn, E.C.Y., and Zelikoff, M., "Absorption
    Coefficients of Oxygen in the Vacuum Ultraviolet," J. Chem. Phys.
    21, 1026-1030 (1953).

5. Lowke, J. J. and Rees, J. A., "The Drift Velocities of Free and
    Attached Electrons in Water Vapor," Aust. J. Phys. 16, 447-453
    (1963).

6. Pack, J. L., Voshall, R. E., and Phelps, A. V., "Drift Velocities of
    Slow Electrons in Krypton, Xenon, Deuterium, Carbon Monoxide, Carbon
    Dioxide, Water Vapor, Nitrous Oxide and Ammonia," Phys. Rev. 127,
    2084-2089 (1962).

7. van Lint, V.A.J., "Electron Mobility and Attachment in Dry and Moist
    Air," Theoretical Note 345, 1 April 1982.

8. Hegerberg, R. and Reid, I. D., "Electron Drift Velocities in Air,"
    Aust. J. Phys. 33, 227-230 (1980).

9. Mentzoni, M. H., "Momentum Transfer Collisions in Oxygen for Thermal
    Electrons," J. Res. Natl. Bur. Std. (U.S.), 69D, 213-217 (1965).

10. Mentzoni, M. H. and Row, R. V., "Rotational Excitation and Electron
    Relaxation in Nitrogen," Phys. Rev. 130, 2312-2316 (1963).

11. Milloy, H. B., Reid, I. D., and Crompton, R. W., "Zero-Field
    Mobility for Electrons in Dry and Humid Air," Aust. J. Phys. 28,
    231-234 (1975).

12. Moruzzi, J. L. and Phelps, A. V., "Survey of Negative-Ion-Molecule Reactions in O_2, CO_2, H_2O, CO and Mixtures of these Gases at High Pressure," J. Chem. Phys. 45, 4617-4627 (1966).

13. Parkes, D. A., "Electron Attachment and Negative-Ion Molecule Reactions in Pure Oxygen," Trans. Faraday Soc. 67, 711-729 (1971).

14. Fehsenfeld, F. C. and Ferguson, E. E., "Laboratory Studies of Negative Ion Reactions with Atmospheric Trace Constituents," J. Chem. Phys. 61, 3181-3193 (1974).

15. Fehsenfeld, F. C., Ferguson, E. E., and Bohme, D. K., "Additional Flowing Afterglow Measurements of Negative Ion Reactions of D-Region Interest," Planet. Space Sci. 17, 1759-1762 (1969).

16. Adams, N. G., Bohme, D. K., Dunkin, D. B., Fehsenfeld, F. C., and Ferguson, E. E., "Flowing Afterglow Studies of Formation and Reactions of Cluster Ions of O_2^+, O_2^- and O^-," J. Chem. Phys. 52, 3133-3140 (1970).

17. Dotan, I., Davidson, J. A., Streit, G. E., Albritton, D. L., and Fehsenfeld, F. C., "A Study of the Reaction $O_3^- + CO_2 \rightarrow CO_3^- + O_2$ and its Implication on the Thermochemistry of CO_3 and O_3 and their Negative Ions," J. Chem. Phys. 67, 2874-2879 (1977).

18. Dunkin, D. B., Fehsenfeld, F. C., and Ferguson, E. E., "Rate Constants for Thermal Energy Reactions of H^- with O_2, NO, CO, and N_2O," J. Chem. Phys. 53, 987-989 (1970).

19. Betowski, D., Payzant, J. D., Mackay, G. I., and Bohme, D. K., "Rate Coefficients at 297 K for Proton Transfer Reactions with H_2O. Comparisons with Classical Theories and Exothermicity," Chem. Phys. Lett. 31, 321-324 (1975).

20. Howard, C. J., Bierbaum, V. M., Rundle, H. W., and Kaufman, F., "Kinetics and Mechanism of the Formation of Water Cluster Ions from O_2^+ and H_2O," J. Chem. Phys. 57, 3491-3497 (1972).

21. Smith, D., Adams, N. G., and Miller, T. M., "A Laboratory Study of the Reactions of N^+, N_2^+, N_3^+, N_4^+, O^+, O_2^+, and NO^+ Ions with Several Molecules at 300 K," J. Chem. Phys. 69, 308-318 (1978).

22. Lindinger, W., McFarland, M., Fehsenfeld, F. C., Albritton, D. L., Schmeltekopf, A. L., and Ferguson, E. E., "Translational and Internal Energy Dependences of Some Ion-Neutral Reactions," J. Chem. Phys. 63, 2175-2181 (1975).

23. Howard, C. J., Rundle, H. W., and Kaufman, F., "Gas-Phase Reaction Rates of Some Positive Ins with Water at 296 K," J. Chem. Phys. 53, 3745-3751 (1970).

24. Fehsenfeld, F. C., Schmeltekopf, A. L., and Ferguson, E. E., "Thermal-Energy Ion-Neutral Reaction Rates. VII. Some Hydrogen-Atom Abstraction Reactions," J. Chem. Phys. 46, 2802-2808 (1967).

25. Good, A., Durden, D. A., and Kebarle, P., "Ion-Molecule Reactions in Pure Nitrogen and Nitrogen Containing Traces of Water at Total Pressures 0.5-4 Torr. Kinetics of Clustering Reactions Forming $H^+(H_2O)_n$," J. Chem. Phys. 52, 212-221 (1970).

26. Good, A., Durden, D. A., and Kebarle, P., "Mechanism and Rate Constants of Ion-Molecule Reactions Leading to Formation of $H^+(H_2O)_n$ in Moist Oxygen and Air," J. Chem. Phys. 52, 222-229 (1970).

27. Hegerberg, R. and Crompton, R. W., "Diffusion, Attachment and Attachment Cooling of Thermal Electrons in Oxygen and Oxygen Mixtures," Aust. J. Phys. 36, 831-844 (1983). A preliminary account of this work is given by R. W. Crompton, R. Hegerberg, and H. R. Skullerud, "Diffusion, Attachment and Attachment Cooling of Thermal Electrons in Molecular Oxygen," Proc. International Seminar on Swarm Experiments in Atomic Collision Research, Tokyo, p. 18-22 (1979).

28. Chanin, L. M., Phelps, A. V., and Biondi, M. A., "Measurements of the Attachment of Low-Energy Electrons to Oxygen Molecules," Phys. Rev. 128, 219-230 (1962).

29. Pack, J. L. and Phelps, A. V., "Electron Attachment and Detachment. I. Pure O_2 at Low Energy," J. Chem. Phys. 44, 1870-1883 (1966).

30. Verhaart, H.F.A. and van der Laan, P.C.T., "The Influence of Water Vapor on Avalanches in Air," J. Appl. Phys. 55, 3286-3292 (1984).

31. Rayment, S. W. and Moruzzi, J. L., "Electron Detachment Studies between O^- Ions and Nitrogen," Int. J. Mass Spec. Ion Phys. 26, 321-326 (1978).

32. Doussot, C., Bastien, F., Marode, E., and Moruzzi, J. L., "A New Technique for Studying Ion Conversion and Detachment Reactions in Oxygen and in O_2/SO_2 and O_2/N_2 Mixtures," J. Phys. D 16, 2451-2461 (1982).

33. Ryzko, H. and Astrom, E., "Electron Attachment-Detachment Processes in Dry Air," J. Appl. Phys. 38, 328-330 (1967).

34. Eccles, M. J., O'Neill, B. C., and Craggs, J. D., "Electron Detachment in Oxygen," J. Phys. B 3, 1724-1731 (1970).

35. O'Neill, B. C. and Craggs, J. D., "Collisional Detachment and Ion Molecule Reactions in Oxygen," J. Phys. B 6, 2625-2633 (1973).

36. Berger, G., "Collisional Detachment Lifetime of Negative Ions in Atmospheric Air," Proc. XV Int. Conf. Phen. Ionized Gases, Minsk, p. 571-572 (1981).

37. Frommhold, L., "Uber verzogerte Elektronen in Elektronenlawinen, insbesondere in Sauerstoff und Luft, durch Bildung und Zerfall negativer Ionen (O$^-$)," Fortschr. Phys. 12, 597-642 (1964).

38. Davies, D. K. and Chantry, P. J., "Air Chemistry Measurements I," Dikewood, Division of Kaman Sciences Corporation, Report No. DC-TN-2030.301-1, October 1982.